

1 **Future permafrost degradation under climate change in a headwater catchment of Central**
2 **Siberia: quantitative assessment with a mechanistic modelling approach**

3 Thibault Xavier¹, Laurent Orgogozo^{1*}, Anatoly S. Prokushkin², Esteban Alonso-González³, Simon
4 Gascoin⁴, Oleg S. Pokrovsky^{1,5}

5 ¹Geoscience Environnement Toulouse (GET), CNRS, UMR5563, Toulouse, 31400, France

6 ²V.N. Sukachev Institute of Forest SB RAS, Russia

7 ³Instituto Pirenaico de Ecología, Consejo Superior de Investigaciones Científicas (IPE-CSIC), Jaca,
8 Spain

9 ⁴Centre d'Etudes Spatiales de la Biosphère, Université de Toulouse, CNRS/CNES/IRD/INRA/UPS,
10 Toulouse, France

11 ⁵BIO-GEO-CLIM Laboratory, Tomsk State University, Tomsk, Russia

12 * *Corresponding author*: Laurent Orgogozo (laurent.orgogozo@get.omp.eu)

13 **Abstract**

14 Permafrost thawing as a result of climate change has major consequences locally and globally for
15 the biosphere as well as for human activities. The quantification of its extent and dynamics under
16 different climate scenarios is needed to design local adaptation and mitigation measures and to bet-
17 ter understand permafrost climate feedbacks. To this end, numerical simulation can be used to ex-
18 plore the response of soil thermal and hydrological regimes to changes in climatic conditions.
19 Mechanistic approaches minimise modelling assumptions by relying on the numerical resolution of
20 continuum mechanics equations, but they involve significant computational effort. In this work, the
21 permaFoam solver is used along with high-performance computing resources to assess the impact
22 of four climate scenarios of the Coupled Model Intercomparison Project Phase 6 (CMIP6) on per-
23 mafrost dynamics within a pristine, forest-dominated watershed in the continuous permafrost zone.
24 Using these century time-scale simulations, changes in the soil temperature, soil moisture, active
25 layer thickness and water fluxes are quantified, assuming no change in the vegetation cover. The
26 most severe scenario (SSP5-8.5) suggests a dramatic increase in both the active layer thickness and
27 annual evapotranspiration, with the maximum values on the watershed in 2100 increasing by +65%
28 and +35% compared to current conditions, respectively. For the active layer thickness, a variable
29 that integrates both the thermal and hydrological states of the near-surface permafrost, this projected
30 increase would correspond to a ~350 km southward shift in current climatic conditions. Moreover,
31 in this scenario, the thermal equilibrium of near-surface permafrost with the new climatic conditions
32 would not be reached in 2100, suggesting a further thawing of permafrost even in the case in which
33 the climate change is halted.

34 **Keywords**

35 Permafrost, climate change, boreal forest, numerical modelling, high performance computing, soil
36 temperature, soil moisture, evapotranspiration.

37

38 **1 Introduction**

39

40 Permafrost is mostly situated in regions that are experiencing especially intense climate
41 change, resulting in widespread warming and thawing, with the shrinking of its lateral extent and
42 the thickening of the soil active layer (Biskaborn et al., 2019; Hu et al., 2022; Li et al.; 2022a, b).
43 Permafrost thawing induces sizable changes in the environment (Walvoord and Kurylyk, 2016;
44 Nitze et al., 2018; Makarieva et al., 2019; Jin et al., 2022; Wright et al., 2022) and for human activi-
45 ties (Shiklomanov et al., 2017; Strelestkiy et al., 2019, 2023; Hjort et al., 2018, 2022) in the Arctic
46 and the sub-Arctic. For instance, a permafrost-thaw-related decrease in the soil moisture leads to an
47 increase in boreal fire frequency (Kurylyk, 2019; Kim et al., 2020), while soil mechanical instabili-
48 ties induced by permafrost thawing threaten human settlements (Ramage et al., 2021) and infra-
49 structure (Bartsch et al., 2021). Moreover, permafrost thaw may exert significant controls on the
50 biogeochemical cycles of carbon and related metals (Sonke et al., 2018; Karlsson et al., 2021;
51 Walvoord and Striegl, 2021) and climate dynamics (Miner et al., 2022; Park and Kug, 2022; de
52 Vrese et al., 2023), with potentially major feedback on climate warming. Thus, anticipating the evo-
53 lution of permafrost cover and dynamics is of primary importance for understanding and mitigating
54 the climate-change-induced impacts at high latitudes. For this, robust and accurate numerical simu-
55 lations are required (Schneider von Deimling et al., 2022; Hu et al., 2023).

56 Boreal forest is one of the largest biomes on Earth (Gauthier et al., 2015), and 80% of its
57 area is located in permafrost regions, and thereby covers 55% of the total global permafrost area
58 (Stuenzi et al., 2021). Due to the complexity of the biophysical processes involved, quantifying the
59 evolution of permafrost dynamics in boreal forests under climate change requires mechanistic, high-
60 resolution modelling approaches (Orgogozo et al., 2019). However, the large extent of the consid-
61 ered areas makes the use of such approaches impracticable at global, continental or regional scales.
62 As a consequence, the mechanistic modelling of permafrost dynamics has to focus on processes at
63 the watershed scale in headwater catchments with long-term environmental monitoring, following a
64 general trend in the Arctic sciences (Speetjens et al., 2023; Vonk et al., 2023). In Arctic environ-

65 ments, the vegetation strongly controls the surface energy budget (Fedorov et al., 2019; Oehri et al.,
66 2022), interacts with climate dynamics (Park et al., 2020; Kirilyanov et al., 2024) and drives water
67 fluxes (Orgogozo et al., 2019). As such, vegetation should be taken into account when simulating
68 the impact of climate warming on permafrost in boreal forest areas (Lorantý et al., 2018, Kirilyanov
69 et al., 2020; Holloway et al., 2020).

70 The quantitative mechanistic modeling of permafrost dynamics under climate change at the head-
71 water catchment scale requires large computational resources, because fine spatio-temporal dis-
72 cretization is needed due to the strong non-linearities and couplings of various physical processes
73 (Kurylyk and Watanabe, 2013). This is especially important for century long simulation periods
74 (O'Neill et al., 2016) and simulation domains with surfaces of up to tens of square kilometres (e.g.
75 Arndal and Torp-Jørgensen, 2020). For this, high performance computing techniques are needed
76 (Orgogozo et al., 2023).

77 In this study, we focus on a permafrost-dominated, forested watershed of central Siberia that
78 was subjected to long-term environmental monitoring, the Kulingdakan watershed (e.g. Prokushkin
79 et al., 2007; Mashukov et al., 2021). The objective is to assess the future state of the permafrost and
80 the ground thermal regime in this continuous-permafrost, boreal forest environment under different
81 climate change scenarios at the century time scale. The permafrost status of this catchment under
82 current climatic conditions has already been investigated (Orgogozo et al., 2019). Here, we simu-
83 late, using a mechanistic modelling approach, the permafrost dynamics at the catchment scale until
84 2100 under various scenarios of climate change. The vegetation controls on permafrost dynamics
85 are partly included in the mechanistic modelling framework, considering evapotranspiration fluxes
86 (Orgogozo et al., 2019), and partly handled empirically, via accounting for the insulating effect of
87 ground-floor vegetation (Blok et al., 2011; Cazaurang et al., 2023). However, because no changes in
88 vegetation are explicitly considered, we assume constant biomass and primary production and
89 therefore investigate only the physical part of the response of permafrost to climate change. We use
90 the permaFoam high performance computing cryohydrogeological simulator (Orgogozo et al.,
91 2023) with a national-level supercomputing infrastructure, the Joliot-Curie supercomputer of the
92 Très Grand Centre de Calcul (TGCC) of the French Alternative Energies and Atomic Energy Com-
93 mission (CEA). The simulated permafrost thawing features in Kulingdakan are discussed and com-
94 pared for different CMIP6 (Coupled Model Intercomparison Project Phase 6) scenarios, including
95 the following:

- 96 - the soil thermal regime (soil temperature and active layer thickness evolution, equivalent south-
- 97 ward shift under current climatic conditions);
- 98 - the soil hydrology (evapotranspiration fluxes and soil moisture evolution);
- 99 - the spatial variability of climate warming impacts at the scale of the watershed under study;
- 100 - the state and evolution of the thermal imbalance of the permafrost (e.g. Ji et al., 2022; Nitzbon et
- 101 al., 2023) in the considered region.

102 **2 Materials and methods**

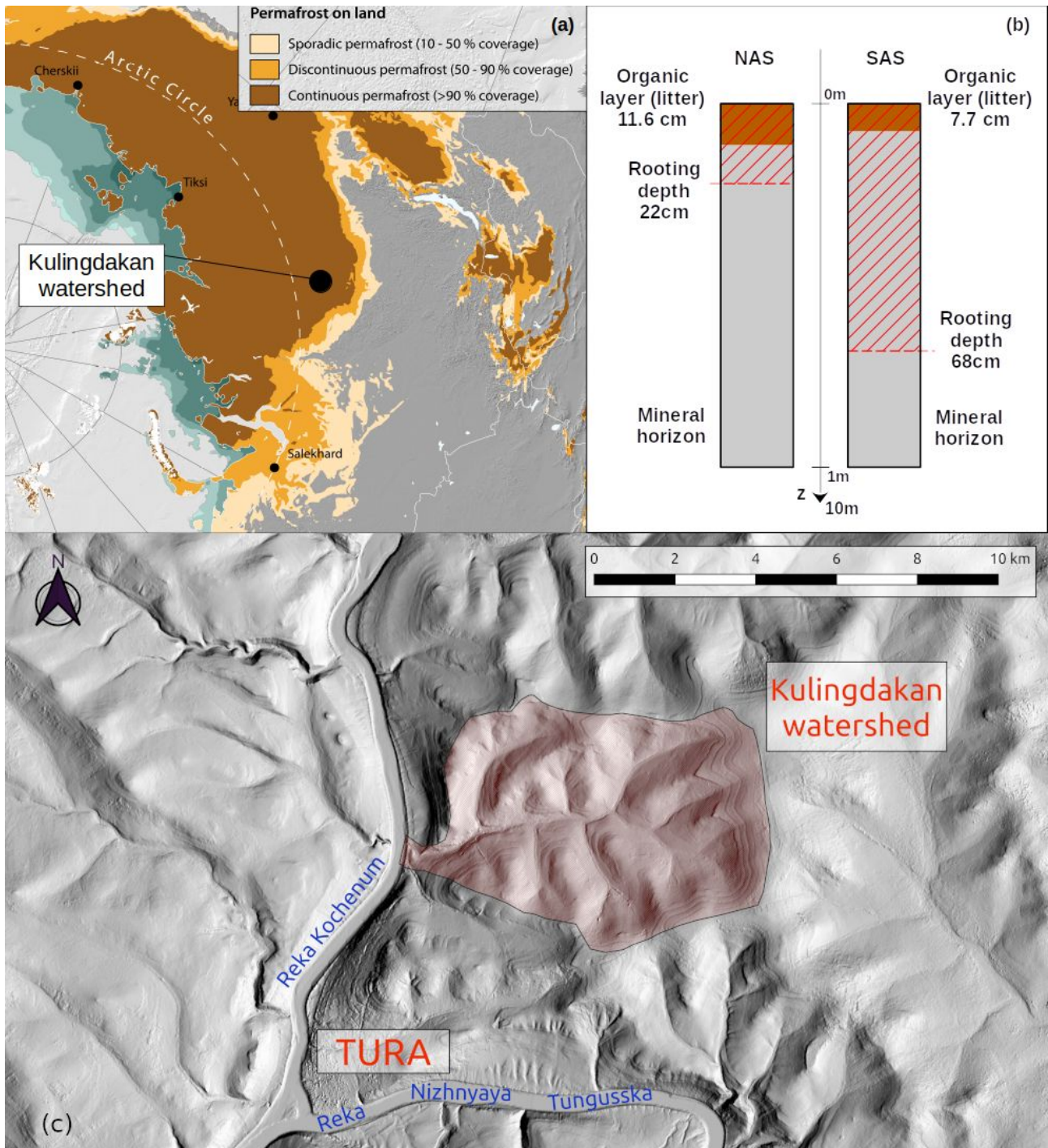
103 **2.1 Study site: Kulingdakan, a forested catchment in continuous-permafrost area**

104 The Kulingdakan catchment is located in the Krasnoïarsk region (64.31°N, 100.28°E),
105 within a continuous permafrost zone, belonging to the boreal forest biome (Northern Taïga – see
106 Fig. 1a). This pristine catchment has been monitored for the study of boreal processes over the past
107 two decades. The vegetation is dominated by larch (*Larix gmelinii*), dwarf shrubs, mosses and
108 lichens. The catchment covers an area of 41 km² and has an elevation ranging from 132 m to 630 m
109 (Prokushkin et al., 2004). The climate is cold and continental, with an average annual mean temper-
110 ature of -8°C and an annual total precipitation of 400 mm (annual mean measured between 1999
111 and 2014 at the Tura meteorological station, 5 km south of the Kulingdakan catchment, altitude of
112 168 m). The stream, which flows from east to west, divides the 41 km² catchment area into two ap-
113 proximately rectangular slopes of equal area, the North Aspect Slope (NAS) and the South Aspect
114 Slope (SAS). As shown by a previous numerical study using permaFoam of this site under current
115 climatic conditions, the hydrological budget in this watershed is largely dominated by evapotranspi-
116 ration fluxes (Orgogozo et al., 2019). Two horizons constitute the soil in the first few metres: an or-
117 ganic horizon (litter and peat) and a mineral horizon (mainly rocky/gravelly loam).

118 Due to the difference in solar radiation induced by their aspects, primary production and
119 evapotranspiration are more intensive in the SAS than in the NAS. Thus the two slopes show signif-
120 icant differences in the larch tree size and larch stand density, as well as in the rooting depth, or-
121 ganic horizon and moss layer thickness and active layer dynamics. The thickness of the organic
122 horizon is 11.6 cm on the NAS and 7.7 cm on the SAS (Gentsch, 2011), while the moss layer thick-
123 ness is 13 cm on the NAS and 6.4 cm on the SAS (Prokushkin et al., 2007). The rooting depth is 10
124 cm into the mineral horizon for the NAS and 60 cm for the SAS (Viers et al., 2013), and this differ-
125 ence has been shown to be of great importance for the dynamics of the active layer (Orgogozo et al.,
126 2019). The observed maximum active layer thickness is 1.22 m in the SAS and 0.58 m in the NAS

127 (Gentsch, 2011). These pedological and physiological contrasts between the two aspects of the wa-
 128 tershed slope, summarised in Figure 1b, are explicitly considered when performing permafrost sim-
 129 ulations (Supplementary Material B – Calculation set-up and details).

130



131 **Figure 1: (a) Location of Kulingdakan watershed (map from GRID-Arendal/Nunataryuk). (b)**
 132 **Representation of soil column structure for North Aspected Slope (NAS) and South Aspected**

133 **Slope (SAS) of the Kulingdakan watershed. (c) Digital Elevation Model (DEM) of Kuling-**
 134 **dakan watershed, extracted from ArcticDEM (Porter et al., 2023).**

135 Previous modelling studies in the Kulingdakan catchment on water flux repartition, the soil
 136 temperature at different depths and the active layer thickness (Orgogozo et al., 2019; Orgogozo et
 137 al., 2023) demonstrated that the use of the permaFoam solver, together with boundary conditions
 138 (water fluxes and soil surface temperature) provided by field measurements, made it possible to ob-
 139 tain numerical simulation results in agreement with in-situ observations under current climatic con-
 140 ditions .

141 **2.2 The permaFoam cryohydrogeological simulator**

142 The numerical tool used in this study is permaFoam (Orgogozo et al., 2019, 2023), the per-
 143 mafrost modelling solver developed in the framework of OpenFOAM, the open source, high perfor-
 144 mance computing tool box for computational fluid dynamics (Weller et al., 1998, openfoam.org,
 145 openfoam.com). This solver is designed to simulate 3D, transient coupled heat and water transfers
 146 in a variably saturated soil with evapotranspiration and the freezing/thawing of the pore water. The
 147 two main equations solved by permaFoam are the Richards equation (Eq. (1)), which governs the
 148 flow of water, and an energy balance equation (Eq. (2)) that governs the heat transfer; both are de-
 149 fined at the Darcy scale of the considered porous medium (soil):

150

$$C_H(h) \frac{\partial h}{\partial t} = \nabla \cdot (K_H(h, T) \cdot \nabla (h+z)) + Q_{AET}(h, t) \quad (1)$$

$$\frac{\partial \left(\left(C_{T,eq}(h, T) + L \frac{\partial \theta_{ice}(h, T)}{\partial T} \right) T \right)}{\partial t} + \nabla \cdot (V(h, T) C_{T,liquid} T) = \nabla \cdot (K_{T,eq}(h, T) \nabla T) \quad (2)$$

151

152 The two primary variables in Eqs, (1) and (2) are the generalised water pressure head h [m] and the
 153 soil temperature T [K], respectively. In the Richards equation (Eq. (1)), z is the vertical coordinate
 154 [m] (oriented upward), K_H is the hydraulic conductivity of the variably saturated, variably frozen
 155 porous medium [$m \cdot s^{-1}$], C_H is the capillary capacity (also called the specific moisture capacity) of
 156 the unsaturated porous medium [m^{-1}] and Q_{AET} [s^{-1}] is a source term representing the water uptake
 157 by vegetation through the evapotranspiration process (computed using the Hamon formula; see Ha-
 158 mon, 1963; Frolking, 1997). From the pressure head field h , the Darcy velocity V [$m \cdot s^{-1}$] is derived
 159 according to Eq. (3):

$$V(h, T) = K_H(h, T) \cdot \nabla(h + z) \quad (3)$$

160

161 In the energy balance equation (Eq. (2)), the considered transfer processes are conduction through
 162 the entire porous medium, convection by pore water flow, and latent heat exchanges when phase
 163 change occurs. In this heat transfer equation, $K_{T,eq}$ [$J \cdot m^{-1} \cdot s^{-1} \cdot K^{-1}$] is the apparent thermal conductivity
 164 of the porous medium, θ_{ice} [-] is the volumetric ice content, L [$J \cdot m^{-3}$] is the latent heat of fusion of
 165 ice, $C_{T,eq}$ [$J \cdot m^{-3} \cdot K^{-1}$] is the equivalent heat capacity of the porous medium, and $C_{T,liquid}$ [$J \cdot m^{-3} \cdot K^{-1}$] is the
 166 equivalent heat capacity of liquid water. In permaFoam these two coupled equations are solved in
 167 3D using the finite volumes method, with sequential operator splitting for handling the couplings,
 168 Picard loops for dealing with the non-linearities and a backward time scheme for temporal discreti-
 169 sation. A detailed description of the solver can be found in Orgogozo et al. (2023).

170 The numerical resolution of these coupled and highly non-linear equations, including stiff
 171 fronts generated by freeze/thaw processes, at the space and time scales required for studying climate
 172 change impacts on boreal watersheds requires both a robust algorithm and the efficient use of high
 173 performance computing means. This is the reason that permaFoam is developed within the Open-
 174 FOAM framework, which allows the use of up-to-date and efficient numerical methods for solving
 175 partial differential equations on last-generation supercomputing facilities. Thanks to its implementa-
 176 tion in OpenFOAM, the permaFoam solver has demonstrated excellent parallel performances on
 177 various supercomputer architectures for dedicated test cases (Orgogozo et al., 2023), both in terms
 178 of large numerical domains (up to 1 billion mesh points on the CALMIP Olympe supercomputer)
 179 and the number of cores (16,000 on the GENCI IRENE-ROME supercomputer).

180

181 **2.3 Modelling domain**

182 According to preliminary numerical experiments (data not shown), for modelling Kuling-
 183 dakan watershed permafrost the use of a dual 2D simplified representation (Orgogozo et al., 2019)
 184 makes it possible to simulate properly the thermal and hydrological fluxes in the soils. As such, full
 185 3D simulations, which are far more costly from a computational perspective than 2D simulations
 186 (Orgogozo et al., 2023), are not needed. Additionally, the use of 2D simulations allows the consid-
 187 eration of lateral transfers (Sjöberg et al., 2016; Lamontagne-Hallé et al.; 2018, Hamm and Framp-
 188 ton, 2021; Jan, 2022). Thus, in this work we used 2D numerical domains, with climatic forcing as
 189 the top boundary conditions (see section 2.4) and geothermal heat flux and nil water flux as the bot-

190 tom boundary conditions. The initial conditions were obtained by 10 years of spin-up under current
191 climatic conditions. These current climatic conditions were represented by a synthetic year of cli-
192 mate forcing corresponding to the multi-annual means of the 1999–2014 observations (see Supple-
193 mentary Material A- Estimating soil surface temperature from external conditions, including Fig.
194 S1). The starting conditions of this spin-up were extracted from the results of the previous calcula-
195 tions (Orgogozo et al., 2019). The convergence criterion for the spin-up was the active layer thick-
196 ness inter-annual difference (annual variability less than 0.2%). The spatial discretisation of the do-
197 main is done using a mesh of 5.2×10^7 cells, according to a convergence study presented in Supple-
198 mentary Material B - Calculation set up and details.

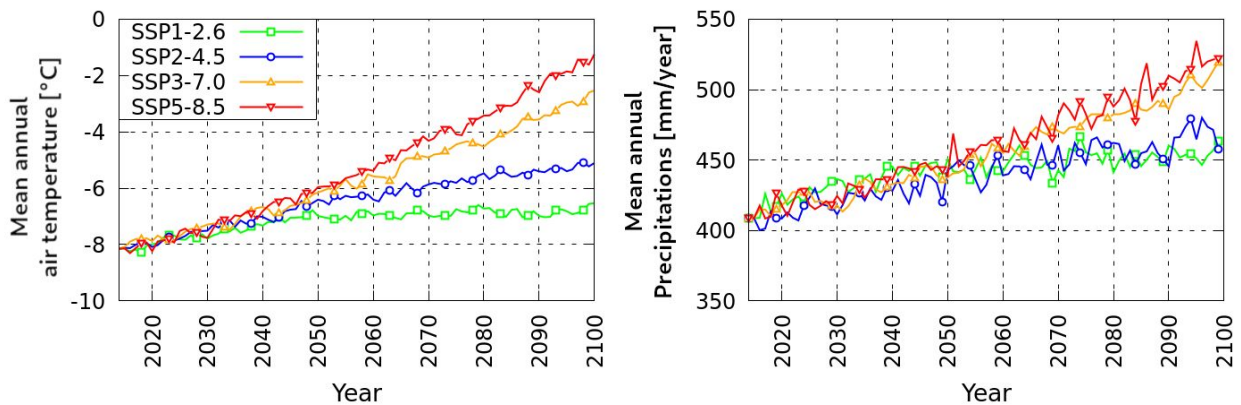
199 The numerical simulations provide the full 2D fields of physical quantities describing the
200 heat and water flow within both the SAS and NAS (two 2.5-km-wide, 10-m-thick slopes), including
201 both the frozen and active layers in each slope. These included the soil temperature, pressure head,
202 liquid water content and ice content for each time step that was saved (user defined; here, every 6
203 months). In addition, the temperature, water content, ice content and evapotranspiration sink term
204 are monitored at an hourly frequency throughout two vertical profiles located at the mid-slope of
205 the SAS and NAS numerical domains, using 61 virtual point probes distributed over the 10 m of the
206 numerical domain thickness. Finally, the infiltration and exfiltration water fluxes through the total
207 soil surface are also saved from the standard output at every time step. Further details of modelling
208 set up are presented in Supplementary Material B – Calculation set up and details..

209 ***2.4 Soil surface conditions under climate change derived from CMIP6 scenarios***

210 In order to apply climate forcings that are representative of possible future trajectories, we
211 consider climate scenarios produced as a part of the Coupled Model Intercomparison Project Phase
212 6 (CMIP6) organised by the Intergovernmental Panel on Climate Change (IPCC) (Eyring et al.,
213 2016); in particular, we consider the so-called tier-1 key scenarios (O’Neill et al., 2016). These sce-
214 narios have been highlighted because of their relevance to scientific questions, the range of possible
215 futures they cover, and their continuity with previous representative common pathways (RCP) sce-
216 narios (van Vuuren et al., 2011) published during CMIP5. We considered four CMIP6 scenarios,
217 from sustainable pathway with the least forcing (coldest) to the pathway with the most forcing
218 (hottest): SSP1-2.6, SSP2-4.5, SSP3-7.0 and SSP5-8.5. Among these scenarios, SSP2-4.5 is the one
219 most often used in permafrost studies (e.g. Karjalainen et al., 2019; Ramage et al., 2021; Hjort et
220 al., 2022). For each of these scenarios, an ensemble of models has been run on different regions of

221 the globe. The climate model output data were accessed via the IPCC Working Group I (IPCC-
 222 WGI) Interactive Atlas (Iturbide et al., 2021), February 2023 version, which provides the median
 223 (P50) of the ensemble of models for a selected output variable, region and scenarios. We used the
 224 projections of the air temperature and precipitation changes for the East Siberian region, averaged at
 225 each yearly time step. To obtain the local scenarios of climate change for the air temperature and
 226 precipitation (Fig. 2), these yearly averaged projections of air temperature / precipitation changes
 227 between 2015 and 2100 have been summed with daily air temperature / precipitation variations
 228 along the synthetic year of climate forcing corresponding to the multi-annual means of the 1999–
 229 2014 observations in Tura, which are representative of current climatic conditions (see Supplemen-
 230 tary Material A - Estimating soil surface temperature from external conditions, Fig. S1). This pro-
 231 vided the projections of the daily air temperature / precipitation from 2015 to 2100 for the Tura
 232 area. The yearly averages of these daily projections are presented in Figure 2.

233



234

235 **Figure 2: Projections of air temperature and precipitation in Kulingdakan based on CMIP6**
 236 **projections on the Eastern Siberia area.**

237 The projections show an increase in the air temperature over the century, with a rate be-
 238 tween $+1.9^{\circ}\text{C}/100$ years (SSP1-2.6) and $+7.8^{\circ}\text{C}/100$ years (SSP5-8.5); these rates were obtained by
 239 re-scaling the averaged increase rates from 2014 to 2100 to the centennial time scale. For every sce-
 240 nario this local increase rate is higher than the global one (global increase rates, according to Fan et
 241 al. [2020]: SSP1-2.6: $+1.18^{\circ}\text{C}/100$ ears; SSP2-4.5: $+3.22^{\circ}\text{C}/100$ years; SSP3-7.0: $+5.50^{\circ}\text{C}/100$
 242 years; SSP5-8.5: $+7.20^{\circ}\text{C}/100$ years). The annual precipitation could also change significantly, with
 243 a relative increase in 2100 of $+12\%$ (SSP1-2.6) to $+29\%$ (SSP5-8.5) compared to the current value.

244 In order to translate these climate projections, which describe atmospheric conditions, into
 245 suitable soil surface boundary conditions for cryohydrogeological simulations (water fluxes and

246 temperature at the soil surface, beneath snow and moss layers), a dedicated empirical procedure has
247 been developed. The goal is to set up a methodology for deriving the soil surface temperature from
248 the air temperature on the slopes of the Kulingdakan watershed, based on the available observation
249 data. Indeed, the soil temperature and air temperature may be significantly different in such a boreal
250 forest environment, due to the effects of understorey (Zellweger et al., 2019; Haesen et al., 2021),
251 moss cover insulation (Blok et al., 2011; Cazaurang et al., 2023), the winter snowpack (Jan and
252 Painter, 2020; Khani et al., 2023) and its interactions with vegetation (Dominé et al., 2022). This
253 empirical, site-specific procedure is detailed in Supplementary Material A - Estimating soil surface
254 temperature from external conditions, and it makes it possible to build up slope-wise soil tempera-
255 ture estimates on the basis of the air temperature and snow conditions. For water fluxes, the sim-
256 plest approximation has been adopted, assuming that the water flux at the top of the soil is equal to
257 the rain flux. For the soil surface temperature estimate, we first used a modified temperature index
258 approach (Braithwaite and Olesen; 1989, Hock 2003) for estimating the snow water equivalent, and
259 then we used multiple regression to derive below-moss soil surface temperature from the air tem-
260 perature, precipitation and snow water equivalent. We chose a temperature index approach to simu-
261 late the snow water equivalent on the soil surface because climate projections only provide the air
262 temperature and precipitation, whereas a more advanced energy balance snowpack model requires
263 additional information on wind, radiation, and air humidity. To calibrate this temperature index
264 model we first reconstruct the snow water equivalent for the period 1999–2014 from the observed
265 snow depth with the Multiple Snow Data Assimilation System (MuSA) toolbox (Alonso-González
266 et al., 2022) forced with ERA5 data (Hersbach et al., 2020), fusing available snow depth observa-
267 tions with an ensemble of simulations generated by the energy and mass balance model called the
268 Flexible Snow Model (Essery, 2015). Then, we calibrated a multiple regression method to derive
269 the soil surface temperature as a function of the air temperature and precipitation, while taking into
270 account the insulating effect of moss and snow layers. Calibrations were performed with air temper-
271 ature and precipitation data measurements, the MuSA-derived snow water equivalent between 1999
272 and 2014 and the top-soil (i.e. below moss) temperature measured in situ between 2003 and 2005.
273 With this procedure, for each slope, an empirical transfer function that provides soil temperature es-
274 timates derived from the air temperature and precipitation was obtained. Finally, these transfer
275 functions were used to produce scenarios of the daily soil surface temperature under climate change
276 for the two slopes of the catchment. This information is to for build the soil surface boundary condi-
277 tions of the hydrogeological simulations. It must be emphasised that our empirical approach was

278 based on parametrical fitting on observation data for estimating the transfer function between atmo-
279 spheric forcing and the soil surface temperature. As a result, no vegetation changes due to climate
280 change could be considered in this transfer function. Therefore, we focus on the purely physical re-
281 sponse of the catchment permafrost to climate change, while considering the vegetation impacts on
282 permafrost dynamics at constant vegetation cover. Coupling a vegetation dynamics with the cryohy-
283 drogeological model would allow one to assess the impact of the climate warming-induced changes
284 of the vegetation cover on permafrost conditions. However, this is beyond the scope of the present
285 study and will be the focus of future work.

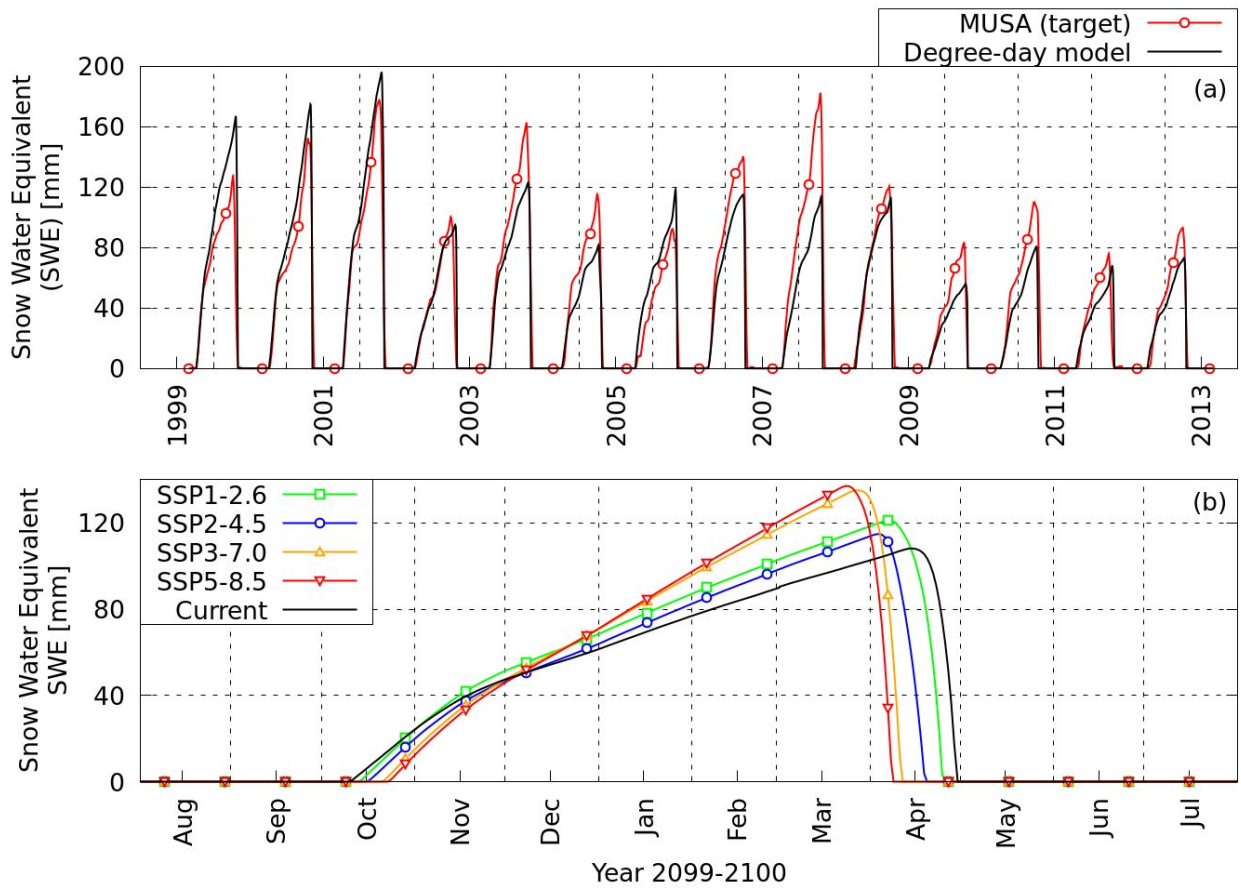
286 **3 Results**

287
288 From post-processing the computed 2D fields of physical quantities describing the heat and water
289 flow within both the SAS and NAS (two 2.5-km-wide, 10-m-thick slopes), including both frozen
290 and active layers in each slope, a large wealth of data characterising the considered virtual per-
291 mafrost dynamics is obtained (Supplementary Material C – Changes in the main variables accord-
292 ing to the four climate projections), and below, only the key features of the centennial evolution un-
293 der climate change are presented.

295 **3.1 Soil surface temperature projections**

296 The results of the temperature index approach used for modelling the snow cover of the Kuling-
297 dakan watershed is presented in Figure 3. The snow water equivalent (SWE) model shows a good
298 agreement with the MuSA reconstructions (Fig. 3a); hence, this model was used to estimate the
299 SWE under future climate projections (Fig. 3b).

300

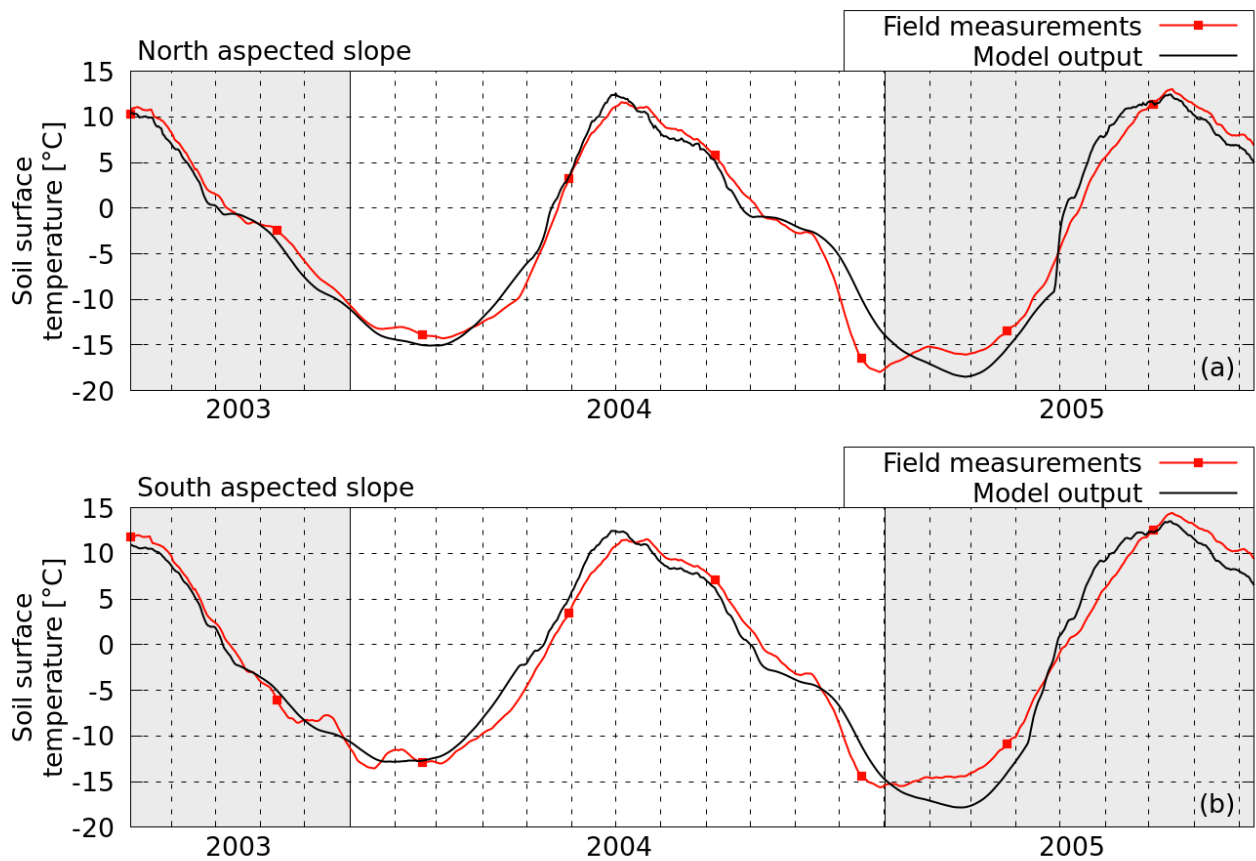


301

302 **Figure 3: (a) Present snow model comparison with MuSA output and (b) projection at the end**
 303 **of the century.**

304 For each slope, the output data of the snow cover model were used as input data for the multiple re-
 305 gression of the soil surface temperature, along with the air temperature data and precipitation data.
 306 These empirical transfer functions were in good agreement with the observations, as shown in Fig-
 307 ure 4.

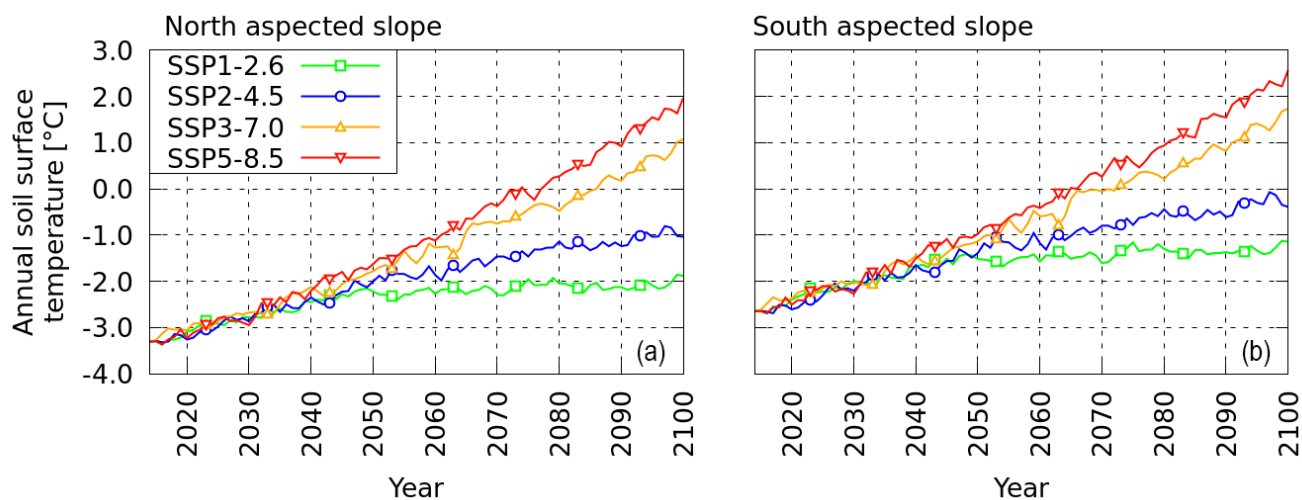
308



309

310 **Figure 4: Measurements and empirical transfer function estimates for soil surface tempera-**
 311 **ture in present climatic conditions in (a) NAS and (b) SAS.**

312 The L1 norm of the differences between the field measurements and model output is 1.42°C in the
 313 NAS, and 1.56°C in the SAS. The L2 norms of these differences are 0.07°C for both the SAS and
 314 NAS. A more detailed discussion of the behaviour of these empirical transfer functions may be
 315 found in Supplementary Material A – Estimating soil surface temperature from external conditions.
 316 Finally, for each slope, soil temperature projections are obtained for the four considered CMIP6 cli-
 317 mate scenarios by applying the developed modelling chain with the projections for air temperature
 318 and precipitation as input data.



319

320 **Figure 5: Soil surface temperature projections over the century based on SSP scenarios ob-**
 321 **tained using the transfer function described in Supplementary Material A – Estimating soil**
 322 **surface temperature from external conditions. Transfer function model estimation for soil**
 323 **surface temperature at present conditions for (a) the NAS and (b) SAS of the Kulingdakan**
 324 **watershed(b).**

325

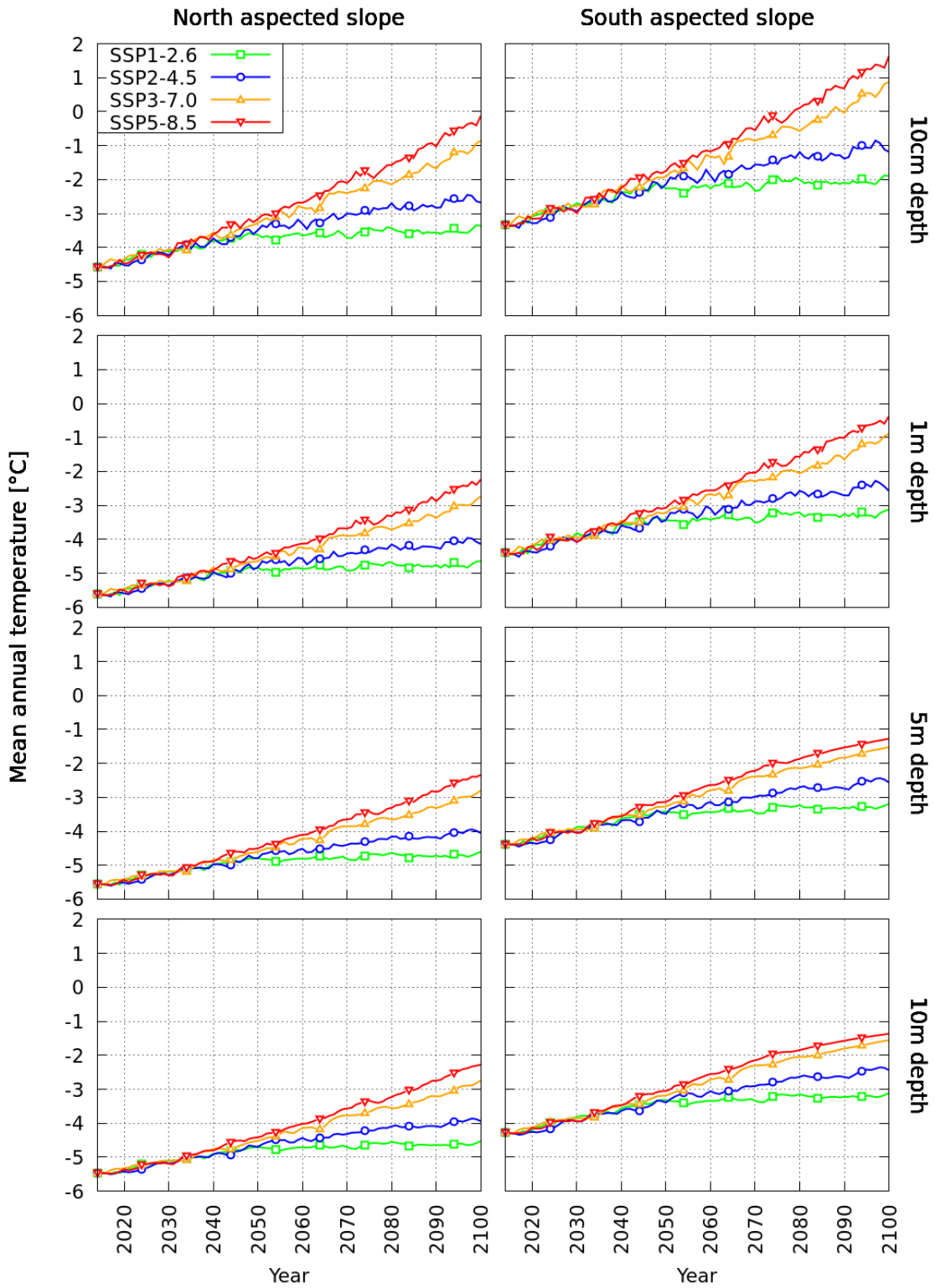
326 The four projections based on the different Shared Socioeconomics Pathways (SSPs) lead to an in-
 327 crease in the ground surface temperature from +1.4°C (SSP1-2.6) to +5.2°C (SSP5-8.5) between
 328 2014 and 2100 (Fig. 5a and 5b). These rates of increase, roughly equivalent by extrapolation to
 329 +1.7°C/100 years (SSP1-2.6) and +5.9°C/100 years (SSP-8.5), are lower than the projected in-
 330 creases in air temperature (+1.9°C/100 years for SSP1-2.6 and +7.8°C/100 years for SSP5-8.5) due
 331 to the insulating effect of the snow cover and the vegetation layer, and also due to the thermal iner-
 332 tia of the soil column below the surface. One can note that for the SSP3-7.0 and SSP5-8.5 scenarios,
 333 the mean annual soil surface temperature becomes positive around 2080.

334 **3.2 Trends in soil temperatures**

335 The soil temperature at different depths is one of the key variables for characterising per-
 336 mafrost dynamics. The multi-annual trends induced by the climate warming of the mean annual soil
 337 temperature between 2014 and 2100 at four depths (10 cm, 1 m, 5 m and 10 m below the surface)
 338 are illustrated in Figure 6.

339

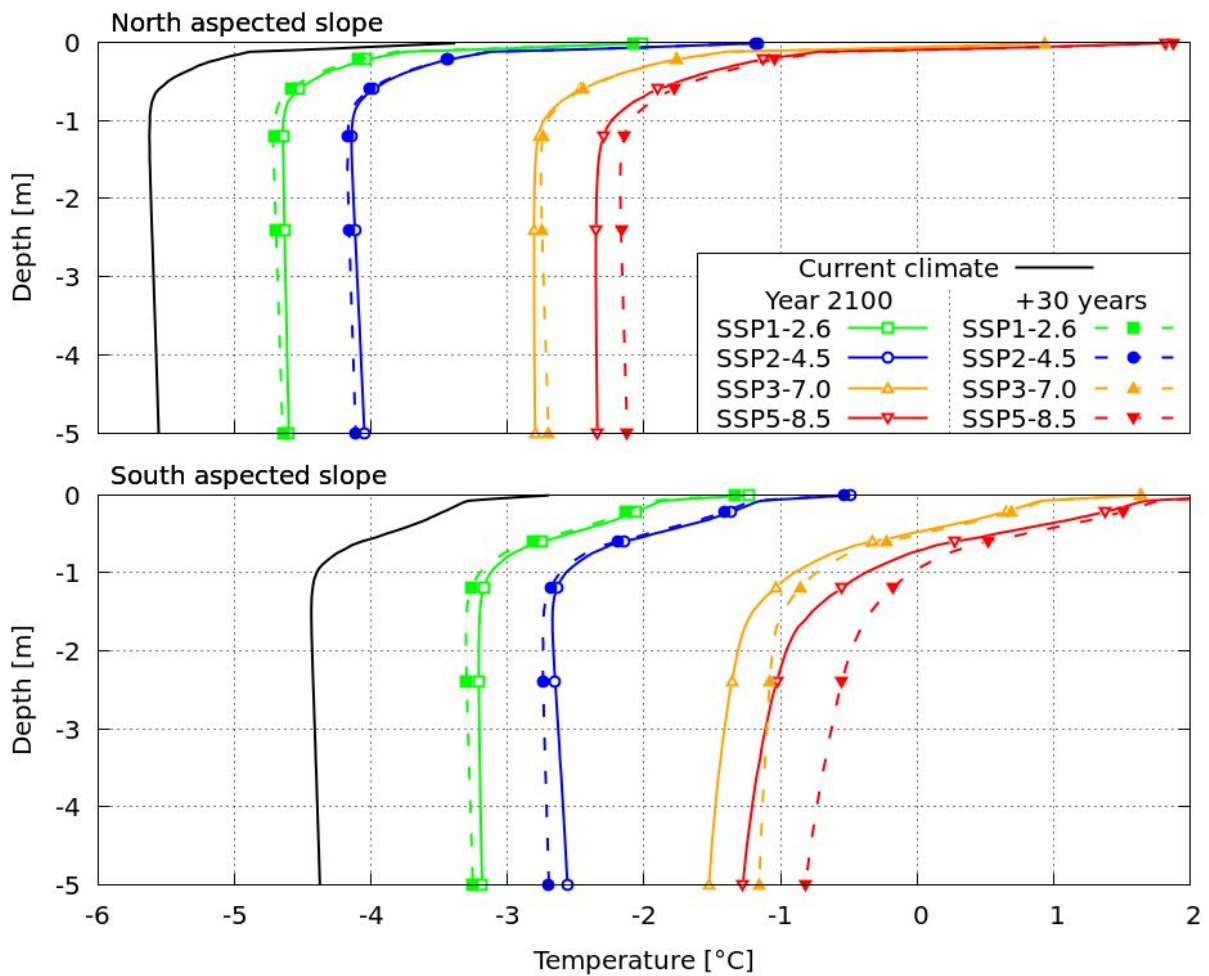
340



341

342 **Figure 6: Mean annual temperature evolution at 10 cm, 1 m, 5 m and 10 m under the surface**
 343 **for each scenario and slope considered.**

344 On both slopes, the soil temperature experiences a significant increase down to 10 m depth,
345 for all climate warming scenarios considered. The annual mean soil temperature even becomes pos-
346 itive close to the surface (10 cm depth) in the SAS for the two high- forcing pathway (hottest) sce-
347 narios, by 2080 for SSP5-8.5 and by 2090 for SSP3-7.0. Meanwhile, for the medium scenario
348 SSP2-4.5 and for the low-forcing sustainable pathway (coldest) scenario SSP1-2.6, the mean annual
349 soil temperature stays negative everywhere until 2100. The warming is more intensive in the SAS
350 than in the NAS, and, as expected, the amplitude of soil warming decreases with depth. In the SAS,
351 at 10 cm depth the temperature rise between current conditions and the year 2100 is 1.4 °C for the
352 SSP1-2.6 scenario and 5.0 °C for the SSP5-8.5 scenario, while at 5 m depth, the temperature rises
353 are 1.2°C and 3.1°C, respectively. In the NAS, at 10 cm depth the temperature rise between current
354 conditions and the year 2100 is 1.2°C for the SSP1-2.6 scenario and 4.4°C for the SSP5-8.5 sce-
355 nario, while at 5 m depth, the temperature rises are 1.0°C and 3.2°C, respectively. It should be noted
356 that, for both slopes, the vertical gradient of the temperature in 2100 is higher in scenario SSP5-8.5
357 than in scenario SSP1-2.6. This indicates a stronger thermal non-equilibrium under more intense
358 warming. For instance, the difference in temperature in 2100 between 10 cm depth and 5 m depth is
359 3.0°C in the SAS and 2.2 °C in the NAS for scenario SSP5-8.5, while it is 1.3°C in the SAS and
360 1.2°C in the NAS for the SSP1-2.6 scenario. In order to provide insight into the thermal equilibrium
361 state of the soil columns in each slope in 2100, additional simulations have been performed by ap-
362 plying the projected climatic conditions of the end of the century (averaged over 2096–2100) for 30
363 more years. For each scenario, the vertical soil temperature profiles for 2100 and for the numerical
364 experiments with 30 more years of 2096–2100 climatic conditions are plotted in Figure 7.



365

366 **Figure 7: Annual mean temperature profiles in 2100 and after 30 years of additional cycling**
 367 **of the average climatic forcing between 2096 and 2100.**

368

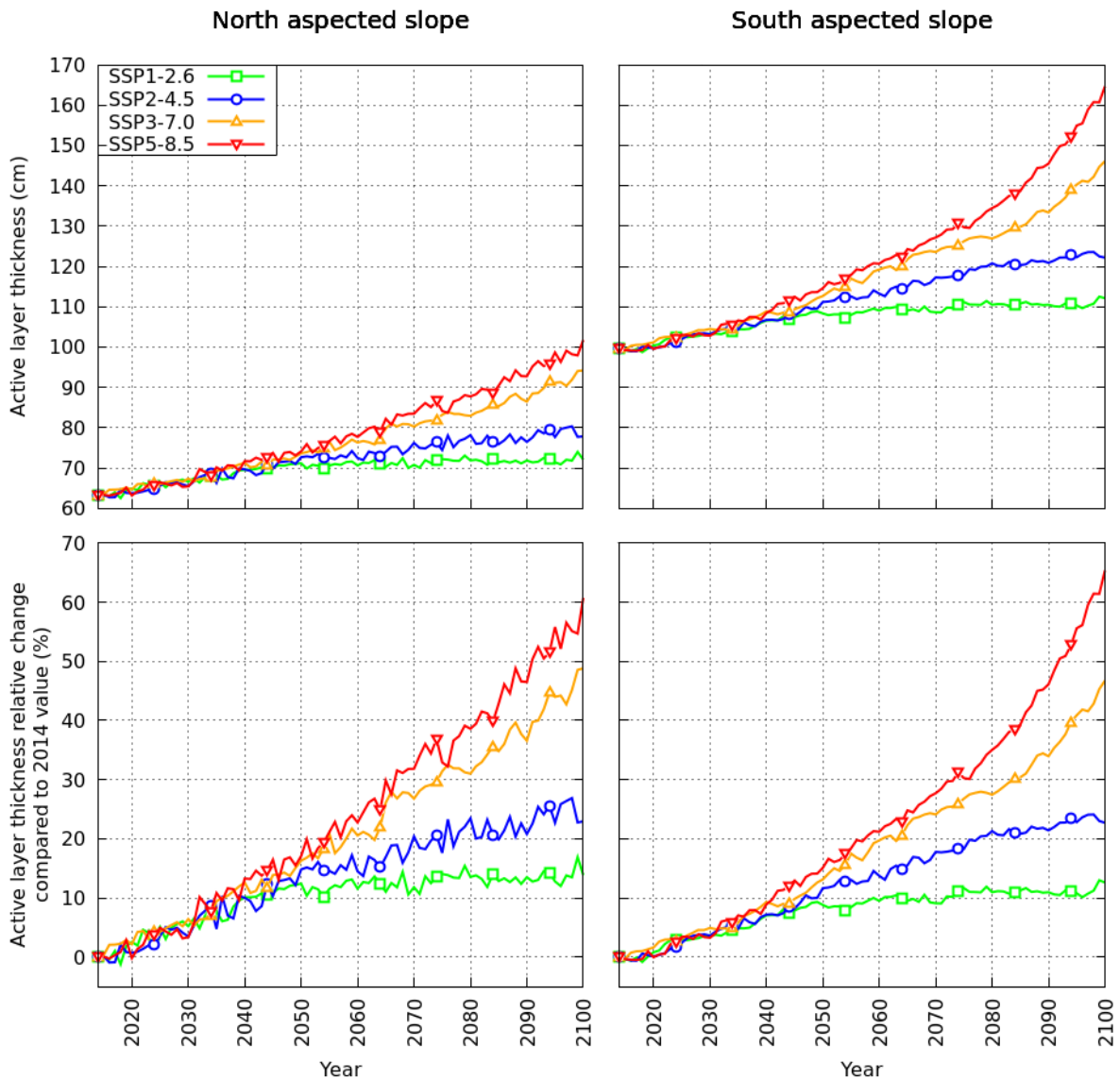
369 Considering the soil temperature profiles in 2100, two regions may be distinguished: the
 370 first metre, with steep positive vertical gradients (the soil surface is warmer than the bottom of the
 371 active layer), and a deeper region, with smoother vertical thermal gradients that are either slightly
 372 negative (SSP1-2.6 and SSP2-4.5 in the NAS and SAS), almost nil (SSP3-7.0 and SSP5-8.5 in the
 373 NAS) or positive (SSP3-7.0 and SSP5-8.5 in the SAS). When comparing these profiles with those
 374 obtained with 30 additional years of modelling in constant ‘2096–2100’ climatic conditions, we ob-
 375 serve important differences in both slopes for scenario SSP5-8.5, and also for scenario SSP3-7.0
 376 and scenario SSP2-4.5, in the SAS.

377

378 **3.3 Active layer thickness evolution**

379 Numerical simulations provide access to the soil temperature at various depths. From the
380 soil temperature profile, the maximum depth with a positive temperature may be computed at each
381 time step. The maximum thawed depth obtained over a year defines the active layer thickness
382 (ALT) of this year. The active layer thickness has been computed for each scenario and each year
383 and is plotted for both the NAS and SAS in Figure 8.

384

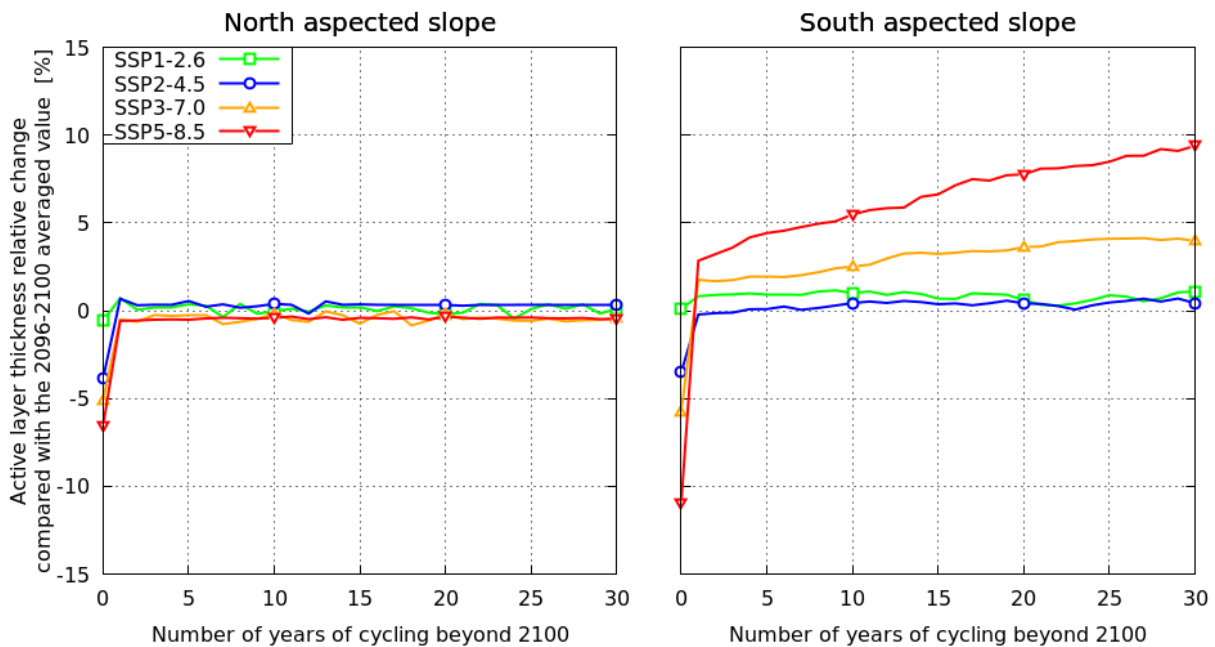


385 **Figure 8: Active layer thickness temporal evolution on the NAS (left) and SAS (right) of the**
386 **Kulingdakan watershed obtained from permaFoam simulations under different SSP scenar-**
387 **ios. Top : Active layer thickness value. Bottom : Relative change compared to 2014 value (63**
388 **cm for NAS, 100 cm for SAS).**

390

391 For both slopes, an increase in the active layer thickness is observed between 2014 and 2100 in every scenario, with a more important thickening in the SAS than in the NAS. SSP1-2.6 leads to an increase of +12.5 cm / +13% for the SAS and +8.8 cm / +14% for the NAS, while SSP5-8.5 leads to a more dramatic increase of +65.1 cm / +65% for the SAS and of +38.5 cm / +61% for the NAS. In the first half of the century, the behaviour of the active layer thickness does not differ significantly between scenarios, with a thickening rate in the ALT of about +3.6 mm/year ($\pm 23\%$) in the SAS and +2.8 mm/year ($\pm 18\%$) in the NAS. However, in the second half of the century (2050–2100), different scenarios lead to very different active layer thickness evolution dynamics. For SSP1-2.6, the thickening rate is rather small, with a rate of +0.60 mm/year for the SAS and +0.32 mm/year for the NAS, while for the SSP5-8.5 scenario, the thickening rate rises to +9.1 mm/year for the SAS and +5.1 mm/year for the NAS. By the end of the simulated period, these thickening rates show no diminishing trend in the SAS, suggesting that the dynamic thermal equilibrium is not reached in the active layer. To illustrate this, Figure 9 shows the active layer thickness evolution for 30 years of additional simulations while keeping the climatic conditions of the end of the century (2096–2100) for each scenario.

406



407

408 **Figure 9: Relative change in active layer thickness compared with the average value for 2096–**
409 **2100 over 30 years of spin-up for a synthetic year obtained by averaging climatic conditions**
410 **between 2096 and 2100.**

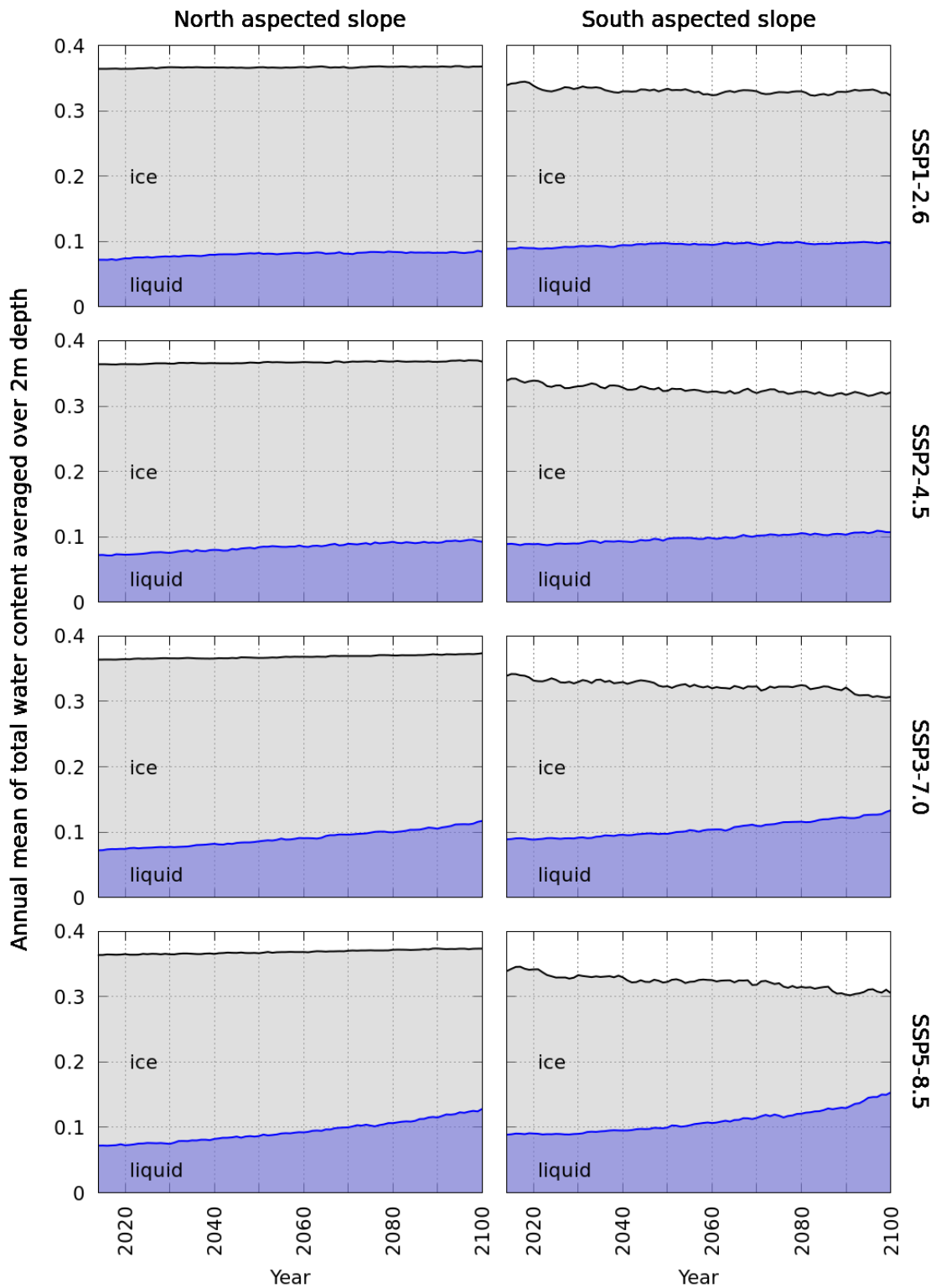
411

412 Overall, the active layer is not far from thermal equilibrium on both slopes for the low-forcing sus-
413 tainable pathway (SSP1-2.6) and medium (SSP2-4.5) climatic scenarios. However, when consider-
414 ing the high-forcing pathway SSP5-8.5 scenario, an important thermal inertia effect appears in the
415 SAS, with an additional active layer thickness increase over these 30 years of +10.4 % compared to
416 the 2096–2100 value, i.e. an increase of +17 cm. This additional change in the active layer thick-
417 ness brings the resulting change compared to the 2014 value to +77 cm (+77%) for the SSP5-8.5
418 scenario for the SAS. The abrupt change observed at the end of the first year of cycling is a direct
419 observation of the abrupt change in climatic forcing (from 2100 forcings to 2096–2100 averaged
420 conditions). Interannual variability is included in CMIP6 scenarios, as can be seen in Figure 2 for
421 both the air temperature and precipitations. For the NAS, the active layer is back to equilibrium in a
422 year, which is a sign of a short response time. For the SAS, and particularly for the steepest scenar-
423 ios, this effect is added to a longer response time change, as discussed previously.

424 **3.4 Trends in soil moisture**

425 The soil moisture content experienced less important changes than the thermal regime under
426 the considered climate change scenario. To illustrate the soil moisture evolution near the surface,
427 the total water, liquid water and ice volumetric contents have been averaged over the first 2 m of the
428 soil for each slopes, and their 2014–2100 evolutions have been plotted in Figure 10 for the four cli-
429 matic scenarios. Note that the 2 m surface soil layer thickness considered for this quantification en-
430 compasses the entire area with water content evolution under the climate change scenarios. Regard-
431 less of the scenario, there is no significant evolution of the total water content in the first 2 m of soil
432 in the NAS, and the only noticeable change is the increase in the proportion of liquid water (+17%
433 in SSP1-2.6, +28 % in SSP2-4.5, +62% in SSP3-7.0, +78% in SSP5-8.5), suggesting an increase in
434 the amount of liquid water available for vegetation. In the SAS, however, the first 2 m of the soil
435 exhibited a slight but detectable diminishing of the total water content by 2100 (-5 % in SSP1-2.6
436 and SSP2-4.5, -10% in SSP3-7.0 and SSP5-8.5). On the other hand, the proportion of liquid water
437 over ice increases (+9% in SSP1-2.6, +20% in SSP2-4.5, +50% in SSP3-7.0, +72% in SSP5-8.5).
438 Therefore, on the SAS, climate warming may result in an increase in the amount of liquid water
439 available for vegetation. This finding is important for heat and water transfers in the soil, given the
440 strong couplings and non-linearities between these transfers. For instance, decreasing the total water
441 content induces a decrease in the soil thermal inertia, while decreasing the share of ice versus liquid
442 water induces a decrease in the apparent thermal conductivity. This can also impact the vegetation

443 dynamics, since vegetation takes up only liquid soil water for transpiration. It should be emphasised
444 that the presented partitioning between liquid water and ice is based on the mean annual quantities.
445 This provides a smaller proportion of liquid water compared to that at the end of the active season
446 (second half of September), when the active layer is at its maximum thickness (see Supplementary
447 material D).

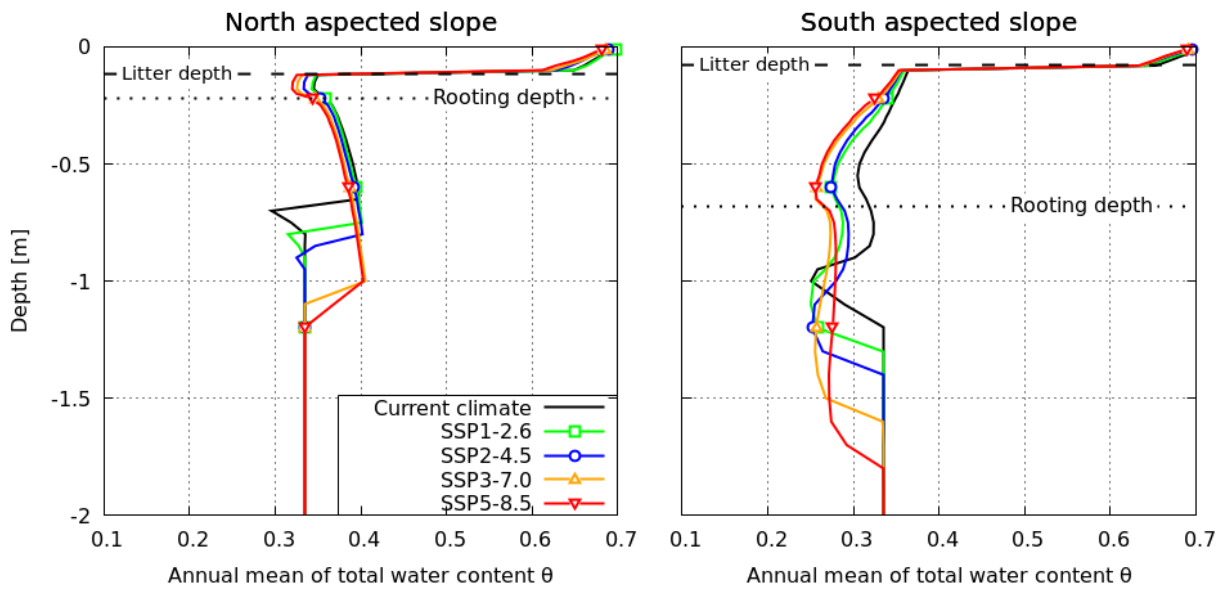


448

449 **Figure 10: Annual mean of total water content [m^3 of water / m^3 of soil] partitioned into liquid**
 450 **(blue) and ice (grey) water content averaged over 2m depth in different climate projections.**

451

452 In order to investigate the local variation of the moisture content in the rooting zone and in
453 the active layer of each slope, the vertical profiles of the mean annual total water content have been
454 plotted in Figure 11 for current climatic conditions and for the year 2100 under the SSP1-2.6, SSP2-
455 4.5, SSP3-7.0 and SSP5-8.5 scenarios. The processes driving the evolution of vertical moisture pro-
456 files are complex; they involve coupled and non-linear heat and water transfers, as well as changing
457 evapotranspiration fluxes. The main changes in the vertical moisture profiles can be described as
458 follows. The water profiles do not change significantly in the highly porous organic horizon for
459 both slopes. In the active layer within the mineral horizon, the behaviors of the SAS and NAS show
460 a greater contrast. In most of the root layers of both slopes, upward vertical moisture gradients, and
461 thus downward water movements, occur. This is likely the signature of an infiltration-dominated
462 flow regime. On the contrary, below the root layer, there are downward vertical moisture
463 gradients, and thus, according to the generalized Darcy's law, upward water movements. This could
464 be explained by the root water uptake occurring above in the root layer, uptake that would create a
465 capillarity-dominated zone where waters are attracted from the depth toward the root layer. SAS
466 and NAS strongly differs in root layer thickness: 10 cm in the mineral horizon in NAS and 60 cm in
467 the mineral horizon in SAS. The shape of the profiles of vertical water fluxes strongly differs be-
468 tween the two slopes, as well as their response to climate change. In the NAS, the only evolution
469 with climate change is a thickening of the zone with a downward vertical moisture gradient (i.e. an
470 upward water flux) alongside the thickening of the active layer, with no significant changes in the
471 gradient itself. Meanwhile, in the SAS, along with the thickening of the zone with water movements
472 (i.e. moisture gradients) that comes with active layer thickening, significant changes in the upward
473 moisture gradients are expected to occur: the hotter the scenario, the steeper the gradients, and thus
474 the stronger the downward water fluxes.



475

476 **Figure 11: Two-meter depth profiles of the annual mean of the total water content [m^3 of wa-**
 477 **ter / m^3 of soil] in 2100: projections compared to current state.**

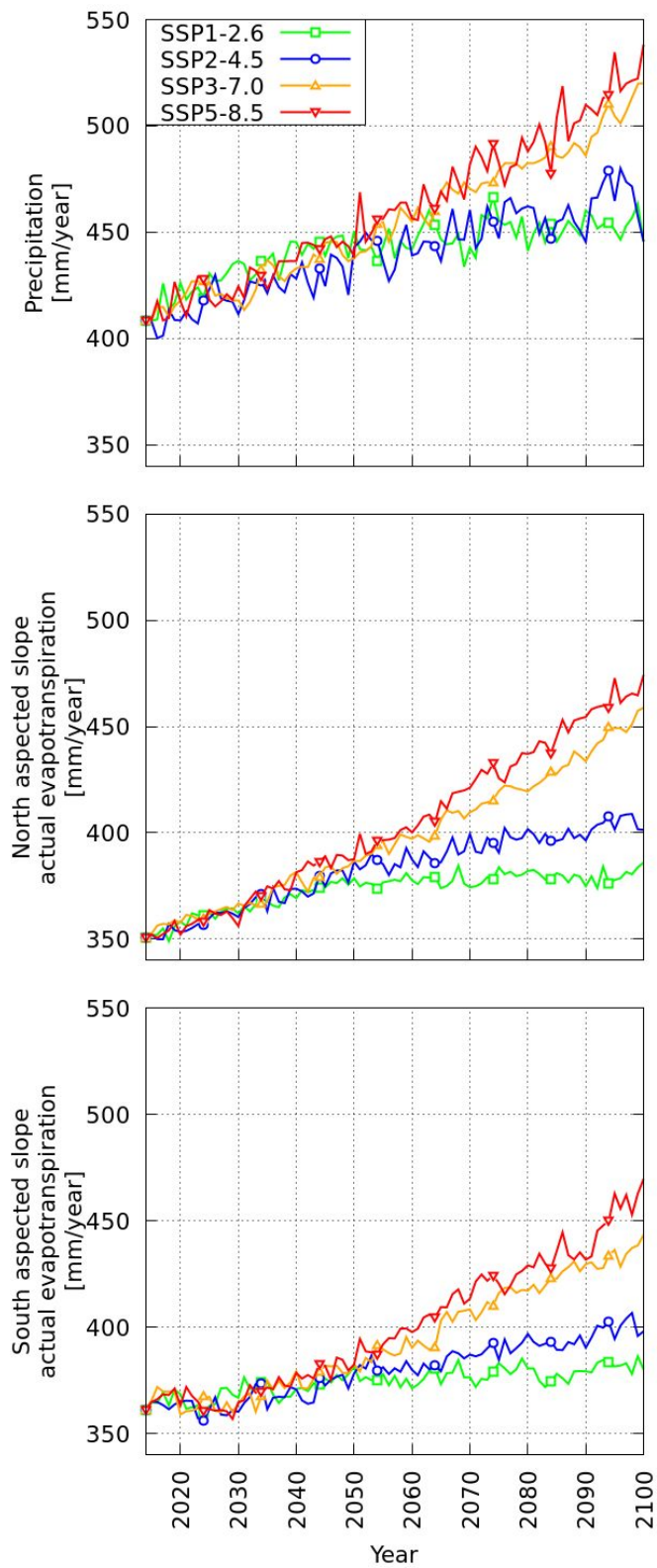
478

479 3.5 Water fluxes

480 The water fluxes also significantly change with climate change on both slopes for every sce-
 481 nario. Evapotranspiration is the most important component of the hydrological budget in Kuling-
 482 dakan. Focusing on this dominant component, Figure 12 presents the centennial evolution of evapo-
 483 transpiration on both slopes and precipitation for the four climate change scenarios. A significant
 484 increase in evapotranspiration is simulated in all cases, with an increase between +19 mm / +5%
 485 (SSP1-2.6) and +108 mm / +30% (SSP5-8.5) in the SAS, and between +35mm / +10% and +123
 486 mm / +35% in the NAS. The increase in the evapotranspiration fluxes in Kulingdakan is correlated
 487 to the increase in precipitation, with similar rates for both slopes.

488

489



490

491 **Figure 12: Precipitation and actual evapotranspiration evolution over the century**

492 Similar to previous simulations of Mean Annual Temperature, soil surface temperature and Active
493 Layer Thickness, the evolution is globally similar among scenarios until 2050, with significant di-
494 vergences appearing only between 2050 and 2100.

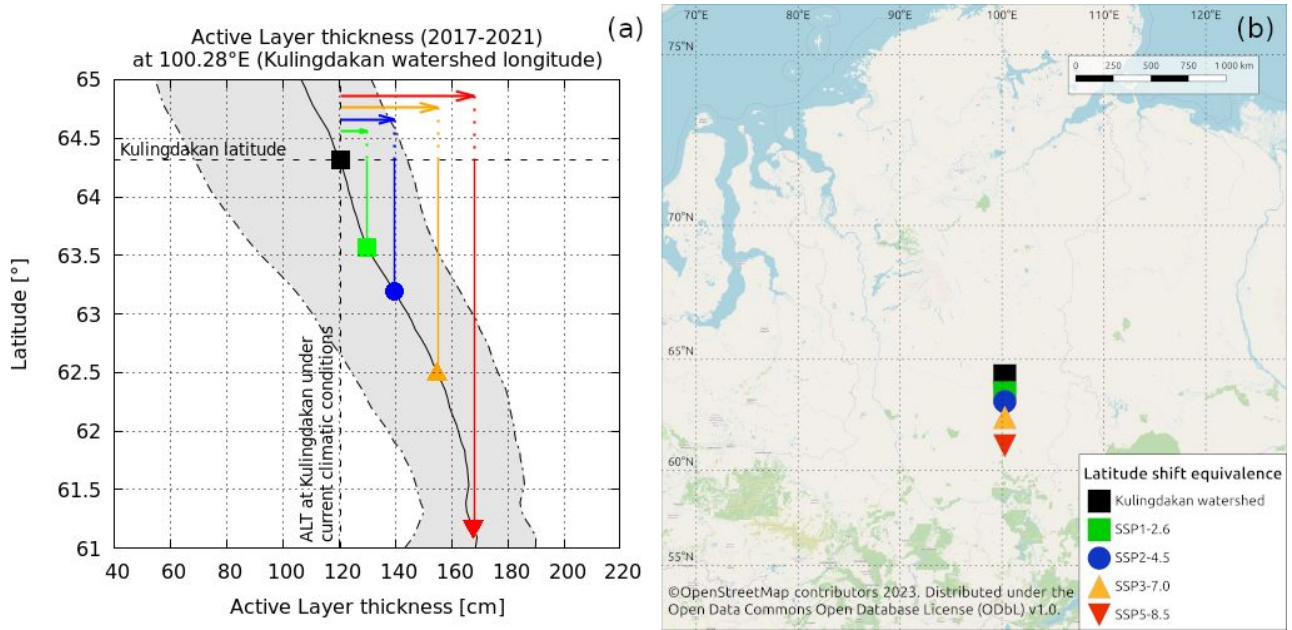
495 **4 Discussion**

496 The numerical results obtained by the mechanistic modelling of heat and water transfer
497 within the permafrost and active layer of Kulingdakan document the physical response to be ex-
498 pected within this catchment under climate change, with soil warming (Fig. 6) and active layer
499 thickening (Fig. 8) in all climate scenarios. An important spatial variability of this thermal response
500 is identified, in relation with the aspect of the slopes, which stems from a sizable contrast in the
501 vegetation cover, hydrologic and thermal state and active layer dynamics, as currently observed be-
502 tween the two slopes of the catchment (Prokushkin et al, 2007). Indeed, since the NAS is wetter, its
503 thermal inertia is more important due to the larger amount of latent heat that must be provided in or-
504 der to thaw and warm its soils, compared to the drier soils of the SAS. This difference in moisture
505 content is largely due to differences in the tree cover biomass and physiology. In particular, the
506 deeper root layer in the SAS compared to the NAS induces more intensive evapotranspiration, un-
507 der both current (Orgogozo et al., 2019) and future climate conditions. Note that this contrast be-
508 tween the two slopes tends to diminish with climate warming (Fig. 12). Liquid water availability for
509 root water uptake is better in SAS than in NAS under current climate as well as in the studied sce-
510 narios of climate change (Supplementary Material D: A view of seasonal change of liquid water
511 available for vegetation uptake). Meanwhile, the SAS is drier than the NAS in terms of total water
512 content in current climate, and this contrast of dryness will increase with climate warming (Fig.
513 10). The pattern of water fluxes within the active layer, with an upward flux to the thinner, close-to-
514 the-surface root layer in the NAS and a downward flux toward the bottom of the thicker root layer
515 in the SAS is also preserved under climate change, with an intensification of the fluxes in the SAS
516 under the high forcing pathway scenarios (Fig. 11). According to Figure 11, the changes in vertical
517 water fluxes will be stronger in the SAS than in NAS, likely due to the pronounced drying of the ac-
518 tive layer of the SAS, while the total water content in the NAS does not change much (Fig. 10). The
519 drying of the root layer in the SAS may then lead to steeper downward moisture gradient and thus
520 more important infiltration flux within this layer. Furthermore, the thicker moss layer in the NAS is
521 likely to alleviate more efficiently the effect of changes in the climatic conditions on soil compared
522 to that in the SAS. Because our modelling takes into account the root water uptake mechanistically

523 (Orgogozo et al., 2023) and the low vegetation insulating effect empirically (Supplementary Mate-
524 rial A – Estimating soil surface temperature from external conditions), the warming of the soil and
525 the thickening of the active layer under climate change are significantly more pronounced in the
526 SAS than in the NAS. This spatial variability in permafrost dynamics of forest environments, per-
527 sistent at all climate change scenarios, reflects the prominent role of micro-climatic conditions in
528 the responses to climate change that has been demonstrated recently in the literature (Zellweger et
529 al., 2020). It must be emphasised that all the numerical results of this study have been obtained con-
530 sidering the vegetation in its present state. The strong local variabilities of the vegetation cover de-
531 pending on the permafrost conditions in the Kulingdakan catchment (Orgogozo et al., 2019) and,
532 from a broader perspective, in the Arctic (Oehri et al., 2022), are consistent with the tight connec-
533 tions between the evolution of vegetation under climate change (e.g. Vitasse et al. 2009, 2011; Rew
534 et al., 2020) and the permafrost pattern, which has not been explicitly considered in this study. At
535 the centennial time scale, changes in the tree growth rate, the forest fire frequency or the nature of
536 the vegetation cover may exert important impacts on permafrost conditions (Cable et al., 2016; Fe-
537 dorov et al., 2019; Rew et al., 2020; Li et al., 2021; Heijmans et al., 2022). Meanwhile, without be-
538 littling these complex interactions between vegetation and permafrost dynamics, this study shows
539 that important impacts of climate change on the permafrost dynamics of the forested continuous
540 permafrost area are to be expected, even with the steady state of the vegetation. We noted that the
541 more intense the climate change, the more pronounced these thermal responses. For instance, under
542 the SSP5-8.5 scenario, a maximum evolution of the active layer thickness is +65 cm / +65% for the
543 SAS and +39 cm / +61% for the NAS, while in the SSP2-4.5 scenario, an increase of +23 cm /
544 +23% for the SAS and of +15 cm / +23% for the NAS is anticipated. Using empirical transfer func-
545 tions to approximate the soil surface temperature from atmospheric conditions under climate change
546 poses the problem of extrapolation, for instance under extreme hot weather conditions that may oc-
547 cur in the future, which are unprecedented in the training period 1999–2014. However, performing
548 the mechanistic modelling of the surface energy balance in extreme weather conditions under per-
549 mafrost contexts was beyond the scope of this work. Additionally, it must be noted that for now in
550 permaFoam, evapotranspiration is assumed to be solely constituted by transpiration, while the evap-
551 oration within the soil is neglected (Orgogozo et al., 2019). This assumption is made in the context
552 of the study of boreal forest areas, in which transpiration largely dominates over evaporation in the
553 hydrological budget (e.g. Park et al., 2021). Meanwhile, evaporation may dominate in tundra envi-
554 ronments (Clark et al., 2023) and likely to increase in the future in forested environments. Since soil

555 evaporation adds another coupling between heat and water transfers through exchanges of latent
 556 heat, it could directly affect the soil temperature evolution. These points should constitute a scope
 557 of future modelling works.

558 To produce a broader geographical context of the active layer thickening projections simu-
 559 lated at the scale of a small catchment, a comparison of centennial evolutions under climate change
 560 with large geographical coverage is performed using a substituting space for time approach (Fig.
 561 13).



562

563 **Figure 13: (a) Equivalence between simulated active layer thickening by 2096–2100 under cli-**
 564 **mate change (SAS and NAS average) and southward latitudinal shift in current climatic con-**
 565 **ditions (2017–2021). – Latitudinal trend (black line – average over a 1°lat. × 1°long. poly-**
 566 **gon) and envelope (in grey – min./max. over years within the same polygon) extracted from Per-**
 567 **mafrost CCI (Westermann et al., 2024). (b) Representation of the latitudinal southward shift**
 568 **equivalent to each climate scenario’s active layer thickening on the regional map.**

569

570 The simulated thickening of the active layer, averaged over both slopes of Kulingdakan, is depicted
 571 as southward latitudinal shifts along the meridian passing by Kulingdakan, i.e. with a north-south
 572 translation along 100.28 °E (Fig. 13). The latitudinal evolution of the active layer thickness along
 573 the current meridian is computed based on the permafrost_CCI dataset (Westermann et al., 2024)
 574 by averaging the value of the multi-annual mean of the active layer thickness for the 2017–2021 pe-
 575 riod over a polygon of 1° of latitude by 1° of longitude centred on the considered meridian and
 576 browsing the latitude between 67°N and 57°N. The 1°-1° polygon was considered big enough to
 577 smooth the small-scale non-homogeneities (at km scale) and small enough to capture the latitudinal

578 effect, including biome transitions (~hundreds of km, e.g. Anisimov et al., 2015) In Figure 13a, the
579 black line describes the multi-annual (1997–2019) temporal average of the spatial average of the ac-
580 tive layer thickness over a 1° - 1° polygon centred on a moving latitude ; the grey shaded area repre-
581 sents the minimum/maximum obtained for this spatial average during the considered period. It can
582 be seen that, in the high-forcing pathway scenario SSP5-8.5, the active layer thickening would cor-
583 respond to a 349 km southward shift, while in the medium scenario SSP2-4.5, it would correspond
584 to a 124 km southward shift.

585 Under a permanently changing climatic context, an important question is the state of thermal
586 equilibrium versus non-equilibrium of the permafrost (Obu et al., 2019): is the climate change in-
587 duced warming slow enough that permafrost may be considered at every time close to the thermal
588 equilibrium with climatic conditions, or on the contrary, do the transient effects dominate the ther-
589 mal dynamics of permafrost under climate change? The simulation results of this work provide in-
590 formation for characterising the degree of thermal equilibrium of the continuous permafrost, in a
591 forested study site under various scenarios of climate change. First of all, we emphasise that, since
592 the bottom thermal boundary condition in our modelling is the geothermal heat flux (Duchkov et
593 al., 1997), the assumption of overall thermal equilibrium at depth (<10 m) in the hundreds of metres
594 of the thick permafrost of the Putorana plateau (Pokrovsky et al., 2005) is implicitly made. Mean-
595 while, the temperature profiles shown in Figure 7 demonstrate that under this assumption the ther-
596 mal equilibrium state of the first 10 m of soil in 2100 depends on both the climate change scenario
597 and the slope aspect. In the NAS, the thermal equilibrium of the first 10 m of soil is achieved by
598 2100 in every climate scenario, with only a slight shift between the 2100 and (2100+30) conditions
599 in the SSP5-8.5 scenario. Additionally, with sub-zero vertical thermal gradients in each scenario,
600 only small heat exchanges between the surface and the deep layer may occur. On the contrary, by
601 2100 in the SAS, strong thermal non-equilibrium is encountered in the two highforcing pathway
602 scenarios, SSP3-7.0 and SSP5-8.5 (Fig. 7 and 8). Under these scenarios, sizable evolutions of tem-
603 perature profiles are expected between 2100 and 2100+30. Moreover, for these two scenarios, the
604 vertical thermal gradients between 1 and 10 m depth are clearly positive (considering an upward
605 vertical axis), which implies an ongoing heat flux from the surface to the depths. In this case, the
606 permafrost is warming below 10 m, at a rate that we implicitly assume to be small enough that it
607 does not modify the total amount of heat stored within this deep permafrost. As such, in scenarios
608 SSP3-7.0 and SSP5-8.5, the climate change clearly induces the transient warming of the permafrost
609 below 10 m depth in the SAS of the Kulingdakan watershed. One could note slightly decreasing

610 trends in the soil temperature under scenarios SSP1-2.6 and SSP2-4.5. This is due to inter-annual
611 variabilities in both the precipitation and air temperature in CMIP6 projections (Fig. 2). Therefore,
612 the year 2100 may offer different conditions from those observed in the 2096-2100 average, which
613 is repeated over 30 cycles to assess the equilibrium state of the permafrost,. For example, in SSP2-
614 4.5, the last decade experiences an important annual precipitation peak, up to 475 mm/year, centred
615 around 2095, before a decreasing trend in the second part of the decade, ending up with a precipita-
616 tion of 410 mm/year projected in 2100. This results, for the year 2100, in a decrease in the snow
617 cover insulating effect in winter and thus a lowering of the soil surface temperature (Fig. 5), com-
618 pared to the conditions encountered in the previous decade.

619 Overall, the results of the present study may be used to improve our understanding of the
620 climate-warming-related changes in the wide areas of boreal forest on continuous permafrost, with
621 implications for continental surfaces (Revich et al., 2022), ecosystems (Wang and Liu 2022) and el-
622 ement cycles (Schuur et al., 2022), and related global consequences and feedbacks. Mechanistic
623 modelling, although it is computationally costly, is capable of providing quantitative information
624 for these research fields. This approach should be applied in other environmentally monitored bo-
625 real watershed, in order to numerically characterise the physical response of permafrost to climate
626 change under various environmental contexts, for instance, in Northern Sweden (Auda et al., 2023)
627 and Western Siberia (Cazaurang et al., 2023).

628 **5 Conclusion**

629 Four main conclusions that could be drawn from this numerical study are the following:

- 630 - All climate change scenarios trigger significant soil warming (+1.8°C in the SAS and +1.5°C in
631 the NAS under the SSP2-4.5 scenario at 1 m depth according to the presented simulations) and an
632 increase in the active layer thickness (+23 cm / +23% in the SAS and +15 cm / +23% in the NAS
633 under the SSP2-4.5 scenario) for both slopes of the Kulingdakan watershed. The projected increase
634 in the active layer thickness under the SSP2-4.5 scenario would be equivalent to a ~120 km south-
635 ward shift in current climatic conditions, and to a ~350 km southward shift under the SSP5-8.5 sce-
636 nario.
- 637 - For all climate change scenarios, the combination of soil warming and an increase in precipitation
638 leads to an important increase in evapotranspiration for both slopes (+37 mm / +10% in the SAS
639 and +51 mm / +14% in the NAS under the SSP2-4.5 scenario). Meanwhile, the mean annual soil
640 moisture decreases only slightly in the NAS (-2.3% under the SSP2-4.5 scenario, averaged over the

641 22 cm of rooting depth), but the decrease is more pronounced in the SAS (-6.0% under the SSP2-
642 4.5 scenario, averaged over the 68 cm of rooting depth).

643 - The important spatial variability observed in the Kulingdakan watershed illustrate the key role of
644 meso-climatic conditions and small-scale geomorphological contrasts in the permafrost response to
645 climate warming

646 - Under the two highforcing pathway scenarios of climate change, SSP3-7.0 and SSP5-8.5, the near-
647 surface permafrost of the SAS of the Kulingdakan watershed is in a non-equilibrium thermal state
648 in 2100, and further investigation is needed to assess whether or not the permafrost below 10 m
649 depth will be close to thermal equilibrium in this region. This indicates the need to develop non-
650 equilibrium modelling approaches for regional and global permafrost modelling under climate
651 change.

652 The approach developed in this study can be applied to other high-latitude permafrost-affected
653 catchments, provided that the necessary information on current thermal and hydrological parameters
654 of the soil as well as vegetation coverage, is available.

655

656 **Data availability**

657 All raw data and simulation cases are accessible via the data portal : <https://hiperborea.omp.eu/> un-
658 der the reference Orgogozo et al., 2024 (dataset).

659 **Author contributions**

660 TX and LO were responsible for the design, implementation and visualisation of the permaFoam
661 simulations. EAG, SG and TX designed and carried out the surface simulations. ASP provided ob-
662 servation data. LO prepared the manuscript with contributions from all co-authors.

663 **Competing interests**

664 The corresponding author has declared that none of the authors has any competing interests.

665

666 **Acknowledgments**

667 This work has been funded by the French National Research Agency ANR (grant no ANR-19
668 CE46-0003-01) and benefited from access to the supercomputers of CALMIP (project p12166) and
669 GENCI (project A0140410794, TGCC). This work was supported by a French government grant
670 managed by the Agence Nationale de la Recherche under the ‘Investissements d’avenir’ program
671 (reference ‘ANR-21-ESRE-0051’). Oleg Pokrovsky is grateful for partial support from the TSU De-
672 velopment Programme PRIORITY – 2030 and project PEACE of PEPR FairCarboN ANR-22-
673 PEXF-0011. Anatoly Prokushkin is supported by State Assignment no. 0287-2021-0008. Esteban
674 Alonso Gonzalez is supported by the European Space Agency through the Climate Change Initia-
675 tive postdoctoral grant.

676 **References**

677 Alonso-González, E., Aalstad, K., Baba, M. W., Revuelto, J., López-Moreno, J. I., Fiddes, J., Es-
678 sery, R., and Gascoin, S.: The Multiple Snow Data Assimilation System (MuSA v1.0), *Geosci.*
679 *Model Dev.*, 15, 9127–9155, <https://doi.org/10.5194/gmd-15-9127-2022>, 2022.

680

681 Anisimov, O. A., Zhiltcova, Y. L., and Razzhivin, V. Y.: Predictive modeling of plant productivity
682 in the Russian Arctic using satellite data, *Izvestiya Atmospheric and Oceanic Physics*, 51(9), 1051–
683 1059, <https://doi.org/10.1134/S0001433815090042>, 2015.

684

685 Arndal, M. F., and Topp-Jørgensen, E. (Eds.): INTERACT Station Catalogue – 2020, DCE – Dan-
686 ish Centre for Environment and Energy, Aarhus University, Denmark, 190 pp., ISBN 978-87-
687 93129-15-3, www.eu-interact.org, 2020.

688

689 Auda, Y., Lundin, E. J., Gustafsson, J., Pokrovsky, O. S., Cazaurang, S., and Orgogozo, L.: A new
690 land cover map of two watersheds under long-term environmental monitoring in the Swedish Arctic
691 using Sentinel-2 data, *Water*, 15, 3311, <https://doi.org/10.3390/w15183311>, 2023.

692

693 Bartsch, A., Pointner, G., Nitze, I., Efimova, A., Jakober, D., Ley, S., Högström, E., Grosse, G., and
694 Schweitzer, P.: Expanding infrastructure and growing anthropogenic impacts along Arctic coasts,
695 *Environ. Res. Lett.*, 16, 115013, <https://doi.org/10.1088/1748-9326/ac3176>, 2021.

696

697 Blok, D., Heijmans, M. M. P. D., Schaepman-Strub, G., Van Ruijven, F., Parmentier, F. J. W., and
698 Maximov, T. C.: The cooling capacity of mosses: Controls on water and energy fluxes in a Siberian
699 tundra site, *Ecosystems*, 14, 1055–1065, <https://doi.org/10.1007/s10021-011-9463-5>, 2011.

700

701 Braithwaite, R. J., and Olesen, O. B.: Calculation of glacier ablation from air temperature, West
702 Greenland, in: *Glacier Fluctuations and Climatic Change*, edited by: Oerlemans, J., Kluwer Aca-
703 demic Publishers, 219–233, 1989.

704

705 Biskaborn, B. K., Smith, S. L., Noetzli, J., *et al.*: Permafrost is warming at a global scale, *Nat.*
706 *Commun.*, 10, 264, <https://doi.org/10.1038/s41467-018-08240-4>, 2019.

707

708 Cable, W. L., Romanovsky, V. E., and Jorgenson, M. T.: Scaling-up permafrost thermal measure-
709 ments in western Alaska using an ecotype approach, *The Cryosphere*, 10, 2517–2532, [https://](https://doi.org/10.5194/tc-10-2517-2016)
710 doi.org/10.5194/tc-10-2517-2016, 2016.

711

712 Cazaurang, S., Marcoux, M., Pokrovsky, O. S., Loiko, S. V., Lim, A. G., Audry, S., Shirokova, L.
713 S., and Orgogozo, L.: Numerical assessment of morphological and hydraulic properties of moss,
714 lichen and peat from a permafrost peatland, *Hydrol. Earth Syst. Sci.*, 27, 431–451, [https://doi.org/](https://doi.org/10.5194/hess-27-431-2023)
715 [10.5194/hess-27-431-2023](https://doi.org/10.5194/hess-27-431-2023), 2023.

716

717 Clark, J. A., Tape, K. D., and Young-Robertson, J. M.: Quantifying evapotranspiration from domi-
718 nant Arctic vegetation types using lysimeters, *Ecohydrology*, 16(1), e2484, 2023.

719

720 De Vrese, P., Georgievski, G., Gonzalez Rouco, J. F., Notz, D., Stacke, T., Steinert, N. J., Wilken-
721 skjeld, S., and Brovkin, V.: Representation of soil hydrology in permafrost regions may explain
722 large part of inter-model spread in simulated Arctic and subarctic climate, *The Cryosphere*, 17,
723 2095–2118, <https://doi.org/10.5194/tc-17-2095-2023>, 2023.

724

725 Dominé, F., Fourteau, K., Picard, G., *et al.*: Permafrost cooled in winter by thermal bridging
726 through snow-covered shrub branches, *Nat. Geosci.*, 15, 554–560, [https://doi.org/10.1038/s41561-](https://doi.org/10.1038/s41561-022-00979-2)
727 022-00979-2, 2022.

728

729 Duchkov, A. D., Sokolova, L. S., Balobaev, V. T., Devyatkin, V. N., Kononov, V. I., and Lysak, S.
730 V.: Heat flow and geothermal field in Siberia, *Geologiya / Geofizika*, 38(11), 1716–1729, 1997.

731

732 Essery, R.: A factorial snowpack model (FSM 1.0), *Geosci. Model Dev.*, 8, 3867–3876, [https://](https://doi.org/10.5194/gmd-8-3867-2015)
733 doi.org/10.5194/gmd-8-3867-2015, 2015.

734

735 Eyring, V., Bony, S., Meehl, G. A., Senior, C. A., Stevens, B., Stouffer, R. J., and Taylor, K. E.:
736 Overview of the Coupled Model Intercomparison Project Phase 6 (CMIP6) experimental design and
737 organization, *Geosci. Model Dev.*, 9, 1937–1958, <https://doi.org/10.5194/gmd-9-1937-2016>, 2016.

738

739 Fan, X., Duan, Q., Shen, C., Wu, Y., and Xing, C.: Global surface air temperatures in CMIP6: His-
740 torical performance and future changes, *Environ. Res. Lett.*, 15, 104056, [https://doi.org/](https://doi.org/10.1088/1748-9326/abb051)
741 [10.1088/1748-9326/abb051](https://doi.org/10.1088/1748-9326/abb051), 2020.

742

743 Fedorov, A. N., Konstantinov, P. Y., Vasilyev, N. F., and Shestakova, A. A., The influence of bo-
744 real forest dynamics on the current state of permafrost in Central Yakutia, *Polar Science*, 22,
745 100483, <https://doi.org/10.1016/j.polar.2019.100483>, 2019.

746

747 Frolking, S.: Sensitivity of spruce/moss boreal forest net ecosystem productivity to seasonal anom-
748 alies in weather, *Journal of Geophysical Research*, 102(D24), 29053–29064, [https://doi.org/](https://doi.org/10.1029/96JD03707)
749 [10.1029/96JD03707](https://doi.org/10.1029/96JD03707), 1997.

750

751 Gauthier, S., *et al.*: Boreal forest health and global change, *Science*, 349, 819–822, [https://doi.org/](https://doi.org/10.1126/science.aaa9092)
752 [10.1126/science.aaa9092](https://doi.org/10.1126/science.aaa9092), 2015.

753

754 Gentsch, N.: Permafrost Soils in Central Siberia: Landscape Controls on Soil Organic Carbon Stor-
755 age in a Light Taiga Biome, Akademische Verlagsgemeinschaft München, Munich, Germany,
756 2011.

757

758 Haesen, S., Lembrechts, J. J., De Frenne, P., Lenoir, J., Aalto, J., Ashcroft, M. B., Kopecký, M.,
759 Luoto, M., Maclean, I., Nijs, I., Niittynen, P., van den Hoogen, J., Arriga, N., Brůna, J., Buchmann,
760 N., Čiliak, M., Collalti, A., De Lombaerde, E., Descombes, P., ... Van Meerbeek, K.: ForestTemp –
761 Sub-canopy microclimate temperatures of European forests, *Global Change Biology*, 27, 6307–
762 6319, <https://doi.org/10.1111/gcb.15892>, 2021.

763

764 Hamm, A., and Frampton, A.: Impact of lateral groundwater flow on hydrothermal conditions of the
765 active layer in a high-Arctic hillslope setting, *The Cryosphere*, 15, 4853–4871, <https://doi.org/10.5194/tc-15-4853-2021>, 2021.

767

768 Hamon, W.R.: Computation of direct runoff amounts from storm rainfall, *International Association*
769 *of Scientific Hydrological Sciences Publication*, 63, 52–62, 1963.

770

771 Heijmans, M. M. P. D., Magnússon, R. Í. Lara, M. J., *et al.*: Tundra vegetation change and impacts
772 on permafrost, *Nat. Rev. Earth Environ.*, 3, 68–84, <https://doi.org/10.1038/s43017-021-00233-0>,
773 2022.

774

775 Hersbach, H., Bell, B., Berrisford, P., Hirahara, S., Horányi, A., Muñoz-Sabater, J., Nicolas, J., Peu-
776 bey, C., Radu, R., Schepers, D., Simmons, A., Soci, C., Abdalla, S., Abellan, X., Balsamo, G.,
777 Bechtold, P., Biavati, G., Bidlot, J., Bonavita, M., De Chiara, G., Dahlgren, P., Dee, D., Diamanta-
778 kis, M., Dragani, R., Flemming, J., Forbes, R., Fuentes, M., Geer, A., Haimberger, L., Healy, S.,
779 Hogan, R. J., Hólm, E., Janisková, M., Keeley, S., Laloyaux, P., Lopez, P., Lupu, C., Radnoti, G.,
780 de Rosnay, P., Rozum, I., Vamborg, F., Villaume, S., and Thépaut, J.-N.: The ERA5 global reanaly-
781 sis, *Q. J. Roy. Meteor. Soc.*, 146, 1999–2049, <https://doi.org/10.1002/qj.3803>, 2020.

782

783 Hjort, J., Karjalainen, O., Aalto, J., *et al.*: Degrading permafrost puts Arctic infrastructure at risk by
784 mid-century, *Nat. Commun.*, 9, 5147, <https://doi.org/10.1038/s41467-018-07557-4>, 2018.

785

786 Hjort, J., Streletskiy, D., Doré, G., *et al.*: Impacts of permafrost degradation on infrastructure, *Nat.*
787 *Rev. Earth Environ.*, 3, 24–38, <https://doi.org/10.1038/s43017-021-00247-8>, 2022.

788

789 Hock, R.: Temperature index melt modelling in mountain areas, *Journal of Hydrology*, 282(1–4),
790 104–115, [https://doi.org/10.1016/S0022-1694\(03\)00257-9](https://doi.org/10.1016/S0022-1694(03)00257-9), 2003.

791

792 Holloway, J. E., Lewkowicz, A. G., Douglas, T. A., *et al.* : Impact of wildfire on permafrost land-
793 scapes: A review of recent advances and future prospects, *Permafrost and Periglac. Process.*, 31,
794 371–382, <https://doi.org/10.1002/ppp.2048>, 2020.

795

796 Hu, G., Zhao, L., Wu, T., Wu, X., Park, H., Li, R., *et al.*: Continued warming of the permafrost re-
797 gions over the Northern Hemisphere under future climate change, *Earth's Future*, 10,
798 e2022EF002835, <https://doi.org/10.1029/2022EF002835>, 2022.

799

800 Hu, G., Zhao, L., Li, R., Park, H., Wu, X., Su, Y., Guggenberger, G., Wu, T., Zou, D., Zhu, X.,
801 Zhang, W., Wu, Y., and Hao, J.: Water and heat coupling processes and its simulation in frozen
802 soils: Current status and future research directions, *CATENA*, 222, 106844, ISSN 0341-8162,
803 <https://doi.org/10.1016/j.catena.2022.106844>, 2023

804

805 Iturbide, M., Fernández, J., Gutiérrez, J. M., Bedia, J., Cimadevilla, E., Díez-Sierra, J., Manzanas,
806 R., Casanueva, A., Baño-Medina, J., Milovac, J., Herrera, S., Cofiño, A. S., San Martín, D., García-
807 Díez, M., Hauser, M., Huard, D., and Yelekci, Ö.: Repository supporting the implementation of
808 FAIR principles in the IPCC-WG1 Atlas, Zenodo, <https://doi.org/10.5281/zenodo.3691645>,
809 <https://github.com/IPCC-WG1/Atlas>, 2022.

810

811 Jan, A., and Painter, S. L.: Permafrost thermal conditions are sensitive to shifts in snow timing, *En-
812 viron. Res. Lett.*, 15, 084026, 2020.

813

814 Jan, A.: Modeling the role of lateral surface flow in low-relief polygonal tundra, *Permafrost and
815 Periglac. Process.*, 33(3), 214–225, <https://doi.org/10.1002/ppp.2145>, 2022.

816

817 Ji, H., Nan, Z., Hu, J., Zhao, Y., and Zhang, Y.: On the spin-up strategy for spatial modeling of per-
818 mafrost dynamics: A case study on the Qinghai-Tibet Plateau, *Journal of Advances in Modeling
819 Earth Systems*, 14, e2021MS002750, <https://doi.org/10.1029/2021MS002750>, 2022.

820

821 Jin, H., Huang, Y., Bense, V. F., Ma, Q., Marchenko, S. S., Shepelev, V. V., Hu, Y., Liang, S.,
822 Spektor, V. V., Jin, X., *et al.*: Permafrost degradation and its hydrogeological impacts, *Water*, 14,
823 372, <https://doi.org/10.3390/w14030372>, 2022.

824

825 Karjalainen, O., Aalto, J., Luoto, M., *et al.*: Circumpolar permafrost maps and geohazard indices for
826 near-future infrastructure risk assessments, *Sci. Data*, 6, 190037, <https://doi.org/10.1038/sdata.2019.37>, 2019.

827

828

829 Karlsson, J., Serikova, S., Vorobyev, S. N., *et al.*: Carbon emission from Western Siberian inland
830 waters. *Nat. Commun.*, 12, 825, <https://doi.org/10.1038/s41467-021-21054-1>, 2021.

831

832 Kim, J.-S., *et al.*: Extensive fires in southeastern Siberian permafrost linked to preceding Arctic Os-
833 cillation, *Sci. Adv.*, 6, eaax3308, <https://doi.org/10.1126/sciadv.aax3308>, 2020.

834

835 Kirilyanov, A.V., Saurer, M., Siegwolf, R., Knorre, A. A., Prokushkin, A. S., Churakova
836 (Sidorova), O. V., Fonti M. V., and Büntgen, U.: Long-term ecological consequences of forest fires
837 in the continuous permafrost zone of Siberia, *Environ. Res. Lett.*, 15, 034061, 2020.

838

839 Kirilyanov, A.V., Saurer, M., Arzac, A., Knorre, A. A., Prokushkin, A. S., Churakova (Sidorova),
840 O. V., Arosio, T., Bechuk, T., Siegwolf, R., and Büntgen, U.: Thawing permafrost can mitigate
841 warming-induced drought stress in boreal forest trees, *Science of the Total Environment*, 912,
842 168858, ISSN 0048-9697, <https://doi.org/10.1016/j.scitotenv.2023.168858>, 2024.

843

844 Khani, H. M., Kinnard, C., Gascoin, S., and Lévesque, E.: Fine-scale environment control on
845 ground surface temperature and thaw depth in a High Arctic tundra landscape, *Permafrost and*
846 *Periglac. Process.*, 34(4), 467–480, <https://doi.org/10.1002/ppp.2203>, 2023.

847

848 Kurylyk, B. L., and Watanabe, K.: The mathematical representation of freezing and thawing pro-
849 cesses in variably-saturated, non-deformable soils, *Advances in Water Resources*, 60, 160–177,
850 ISSN 0309-1708, <https://doi.org/10.1016/j.advwatres.2013.07.016>, 2013.

851

852 Kurylyk, B. L.: Engineering challenges of warming, *Nat. Clim. Chang.*, 9, 807–808, [https://](https://doi.org/10.1038/s41558-019-0612-8)
853 doi.org/10.1038/s41558-019-0612-8, 2019.

854

855 Lamontagne-Hallé, P., McKenzie, J. M., Kurylyk, B. L., and Zipper, S.C.: Changing groundwater
856 discharge dynamics in permafrost regions, *Environ. Res. Lett.*, 13, 084017, 2018.

857

858 Li, X.-Y., Jin, H.-J., Wang, H.-W., Marchenko, S. S., Shan, W., Luo, D.-L., He, R.-X., Spektor, V.,
859 Huang, Y.-D., Li, X.-Y., and Jia, N.: Influences of forest fires on the permafrost environment: A re-
860 view, *Advances in Climate Change Research*, 12(1), 48–65, ISSN 1674-9278, [https://doi.org/](https://doi.org/10.1016/j.accre.2021.01.001)
861 [10.1016/j.accre.2021.01.001](https://doi.org/10.1016/j.accre.2021.01.001), 2021.

862

863 Li, G., Zhang, M., Pei, W., Melnikov, A., Khristoforov, I., Li, R., and Yu, F.: Changes in per-
864 mafrost extent and active layer thickness in the Northern Hemisphere from 1969 to 2018, *Science of*
865 *the Total Environment*, 804, 150182, ISSN 0048-9697, [https://doi.org/10.1016/](https://doi.org/10.1016/j.scitotenv.2021.150182)
866 [j.scitotenv.2021.150182](https://doi.org/10.1016/j.scitotenv.2021.150182), 2022a.

867

868 Li, C., Wei, Y., Liu, Y., Li, L., Peng, L., Chen, J., *et al.*: Active layer thickness in the Northern
869 Hemisphere: Changes from 2000 to 2018 and future simulations, *Journal of Geophysical Research:*
870 *Atmospheres*, 127, e2022JD036785, <https://doi.org/10.1029/2022JD036785>, 2022b.

871

872 Loranty, M. M., Abbott, B. W., Blok, D., Douglas, T. A., Epstein, H. E., Forbes, B. C., Jones, B.
873 M., Kholodov, A. L., Kropp, H., Malhotra, A., Mamet, S. D., Myers-Smith, I. H., Natali, S. M.,
874 O'Donnell, J. A., Phoenix, G. K., Rocha, A. V., Sonnentag, O., Tape, K. D., and Walker, D. A.: Re-
875 views and syntheses: Changing ecosystem influences on soil thermal regimes in northern high-lati-
876 tude permafrost regions, *Biogeosciences*, 15, 5287–5313, <https://doi.org/10.5194/bg-15-5287-2018>,
877 2018.

878

879 Makarieva, O., Nesterova, N., Post, D. A., Sherstyukov, A., and Lebedeva, L.: Warming tempera-
880 tures are impacting the hydrometeorological regime of Russian rivers in the zone of continuous per-
881 mafrost, *The Cryosphere*, 13, 1635–1659, <https://doi.org/10.5194/tc-13-1635-2019>, 2019.

882

883 Mashukov, D. A., Benkova, A. V., Benkova, V. E., *et al.*: Radial growth and anatomic structure of
884 the trunk wood of healthy and stag-headed larch trees on permafrost, *Contemp. Probl. Ecol.*, 14,
885 767–774, <https://doi.org/10.1134/S1995425521070143>, 2021.

886

887 Miner, K. R., Turetsky, M. R., Malina, E., *et al.*: Permafrost carbon emissions in a changing Arctic,
888 *Nat. Rev. Earth Environ.*, 3, 55–67, <https://doi.org/10.1038/s43017-021-00230-3>, 2022.

889

890 Nitzbon, J., Krinner, G., Schneider von Deimling, T., Werner, M., and Langer, M.: First quantifica-
891 tion of the permafrost heat sink in the Earth’s climate system, *Geophysical Research Letters*, 50,
892 e2022GL102053, <https://doi.org/10.1029/2022GL102053>, 2023.

893

894 Nitze, I., Grosse, G., Jones, B. M., *et al.*: Remote sensing quantifies widespread abundance of per-
895 mafrost region disturbances across the Arctic and Subarctic, *Nat. Commun.*, 9, 5423, [https://](https://doi.org/10.1038/s41467-018-07663-3)
896 doi.org/10.1038/s41467-018-07663-3, 2018.

897

898 Obu, J., Westermann, S., Bartsch, A., Berdnikov, N., Christiansen, H. H., Dashtseren, A., Delaloye,
899 R., Elberling, B., Etzelmüller, B., Kholodov, A., Khomutov, A., Kääh, A., Leibman, M. O.,
900 Lewkowicz, A. G., Panda, S. K., Romanovsky, V., Way, R. G., Westergaard-Nielsen, A., Wu, T.,
901 Yamkhin, J., and Zou, D., Northern Hemisphere permafrost map based on TTOP modelling for
902 2000–2016 at 1 km² scale, *Earth-Science Reviews*, 193, 299–316, ISSN 0012-8252, [https://](https://doi.org/10.1016/j.earscirev.2019.04.023)
903 doi.org/10.1016/j.earscirev.2019.04.023, 2019.

904

905 Oehri, J., Schaepman-Strub, G., Kim, J. S., *et al.*: Vegetation type is an important predictor of the
906 arctic summer land surface energy budget, *Nat. Commun.*, 13, 6379, [https://doi.org/10.1038/](https://doi.org/10.1038/s41467-022-34049-3)
907 [s41467-022-34049-3](https://doi.org/10.1038/s41467-022-34049-3), 2022.

908

909 O’Neill, B. C., Tebaldi, C., van Vuuren, D. P., Eyring, V., Friedlingstein, P., Hurtt, G., Knutti, R.,
910 Kriegler, E., Lamarque, J.-F., Lowe, J., Meehl, G. A., Moss, R., Riahi, K., and Sanderson, B. M.:
911 The Scenario Model Intercomparison Project (ScenarioMIP) for CMIP6, *Geosci. Model Dev.*, 9,
912 3461–3482, <https://doi.org/10.5194/gmd-9-3461-2016>, 2016.

913

914 Orgogozo, L., Prokushkin, A. S., Pokrovsky, O. S., Grenier, C., Quintard, M., Viers, J., and Audry,
915 S.: Water and energy transfer modeling in a permafrost-dominated, forested catchment of Central
916 Siberia: The key role of rooting depth, *Permafrost and Periglacial Processes*, 30, 75–89, [https://](https://doi.org/10.1002/ppp.1995)
917 doi.org/10.1002/ppp.1995, 2019.

918

919 Orgogozo, L., Xavier, T., Oulbani, H., and Grenier, C.: Permafrost modelling with OpenFOAM®:
920 New advancements of the permaFoam solver, *Computer Physics Communications*, 282, [https://](https://doi.org/10.1016/j.cpc.2022.108541)
921 doi.org/10.1016/j.cpc.2022.108541, 2023.

922

923 Orgogozo, L. & Xavier, T. (). Permafrost mechanistical simulation with the permaFoam solver in
924 the Kulingdakan watershed (Central Siberia) based on CMIP6 scenarios (2014-2100). [dataset].
925 Theia. <https://doi.org/10.6096/1026>, 2024.

926

927 Park, H., Tanoue, M., Sugimoto, A., Ichianagi, K., Iwahana, G., and Hiyama, T.: Quantitative sep-
928 aration of precipitation and permafrost waters used for evapotranspiration in a boreal forest: A nu-
929 merical study using tracer model, *Journal of Geophysical Research: Biogeosciences*, 126,
930 e2021JG006645, <https://doi.org/10.1029/2021JG006645>, 2021.

931

932 Park, S. W., Kim, J. S., and Kug, J. S.: The intensification of Arctic warming as a result of CO₂
933 physiological forcing, *Nat. Commun.*, 11, 2098, <https://doi.org/10.1038/s41467-020-15924-3>, 2020.

934

935 Park, S. W., and Kug, J. S.: A decline in atmospheric CO₂ levels under negative emissions may en-
936 hance carbon retention in the terrestrial biosphere, *Commun. Earth Environ.*, 3, 289, [https://](https://doi.org/10.1038/s43247-022-00621-4)
937 doi.org/10.1038/s43247-022-00621-4, 2022.

938

939 Pokrovsky, O. S., Schott, J. S., Kudryavtzev, D. I., and Dupré, B.: Basalt weathering in Central
940 Siberia under permafrost conditions, *Geochimica et Cosmochimica Acta*, 69(24), 5659–5680, 2005.

941

942 Porter, C., Howat, I., Noh, M.-J., Husby, E., Khuvis, S., Danish, E., Tomko, K., Gardiner, J., Ne-
943 grete, A., Yadav, B., Klassen, J., Kelleher, C., Cloutier, M., Bakker, J., Enos, J., Arnold, G., Bauer,
944 G., and Morin, P., ArcticDEM - Mosaics, Version 4.1, Harvard Dataverse, V1, [https://doi.org/](https://doi.org/10.7910/DVN/3VDC4W)
945 [10.7910/DVN/3VDC4W](https://doi.org/10.7910/DVN/3VDC4W), 2023.

946

947 Prokushkin, A., Kajimoto, T., Prokushkin, S., McDowell, W., Abaimov, A. P., and Matsuura, Y.:
948 Climatic factors influencing fluxes of dissolved organic carbon from the forest floor in a continu-
949 ous-permafrost Siberian watershed, *Canadian Journal of Forest Research-Journal Canadien de la*
950 *Recherche Forestiere*, 35, 2130–2140, <https://doi.org/10.1139/x05-150>, 2004.

951

952 Prokushkin, A. S., Gleixner, G., McDowell, W. H., Ruehlow, S., and Schulze, E.-D.: Source- and
953 substrate-specific export of dissolved organic matter from permafrost-dominated forested watershed
954 in central Siberia, *Global Biogeochem. Cycles*, 21, GB4003, [https://doi.org/](https://doi.org/10.1029/2007GB002938)
955 [10.1029/2007GB002938](https://doi.org/10.1029/2007GB002938), 2007.

956

957 Ramage, J., Jungsberg, L., Wang, S., *et al.*: Population living on permafrost in the Arctic, *Popul.*
958 *Environ.*, 43, 22–38, <https://doi.org/10.1007/s11111-020-00370-6>, 2021.

959

960 Revich, B. A., Eliseev, D. O., and Shaposhnikov, D. A.: Risks for public health and social infra-
961 structure in Russian Arctic under climate change and permafrost degradation, *Atmosphere*, 13, 532,
962 <https://doi.org/10.3390/atmos13040532>, 2022.

963

964 Rew, L. J., McDougall, K. L., Alexander, J. M., Daehler, C. C., Essl, F., Haider, S., Kueffer, C.,
965 Lenoir, J., Milbau, A., Nuñez, M. A., Pauchard, A., and Rabitsch, W.: Moving up and over: Redis-
966 tribution of plants in alpine, Arctic, and Antarctic ecosystems under global change, *Arctic, Antarc-*
967 *tic, and Alpine Research*, 52(1), 651–665, <https://doi.org/10.1080/15230430.2020.1845919>, 2020.

968

969 Schneider von Deimling, T., Lee, H., Ingeman-Nielsen, T., Westermann, S., Romanovsky, V., Lam-
970 oureux, S., Walker, D. A., Chadburn, S., Trochim, E., Cai, L., Nitzbon, J., Jacobi, S., and Langer,
971 M.: Consequences of permafrost degradation for Arctic infrastructure – bridging the model gap be-
972 tween regional and engineering scales, *The Cryosphere*, 15, 2451–2471, [https://doi.org/10.5194/tc-](https://doi.org/10.5194/tc-15-2451-2021)
973 [15-2451-2021](https://doi.org/10.5194/tc-15-2451-2021), 2021.

974

975 Schuur, E.A.G., *et al.*: Permafrost and climate change: Carbon cycle feedbacks from the warming
976 Arctic, *Annual Review of Environment and Resources*, 47(1), 343–371, 2022.

977

978 Shiklomanov, N. I., Streletskiy, D. A., Swales, T. B., and Kokorev, V. A.: Climate change and sta-
979 bility of urban infrastructure in Russian permafrost regions: Prognostic assessment based on GCM

980 climate projections, *Geographical Review*, 107(1), 125–142, <https://doi.org/10.1111/gere.12214>,
981 2017.

982

983 Sjöberg, Y., Coon, E., Sannel, A. B. K., Pannetier, R., Harp, D., Frampton, A., Painter, S. L., and
984 Lyon, S. W.: Thermal effects of groundwater flow through subarctic fens: A case study based on
985 field observations and numerical modeling, *Water Resour. Res.*, 52, 1591–1606, [https://doi.org/](https://doi.org/10.1002/2015WR017571)
986 [10.1002/2015WR017571](https://doi.org/10.1002/2015WR017571), 2016.

987

988 Sonke, J. E., Teisserenc, R., Heimbürger-Boavida, L.-E., Petrova, M. V., Maruszczak, N., Le Dantec,
989 T., Chupakov, A. V., Li, C., Thackray, C. P., Sunderland, E. M., Tananaev, N., and Pokrovsky, O.
990 S.: Eurasian river spring flood observations support net Arctic Ocean mercury export to the atmos-
991 phere and Atlantic Ocean, *PNAS*, 115, 50, E11586–E11594, [www.pnas.org/cgi/doi/10.1073/](http://www.pnas.org/cgi/doi/10.1073/pnas.1811957115)
992 [pnas.1811957115](http://www.pnas.org/cgi/doi/10.1073/pnas.1811957115), 2018.

993

994 Speetjens, N. J., Hugelius, G., Gumbrecht, T., Lantuit, H., Berghuijs, W. R., Pika, P. A., Poste, A.,
995 and Vonk, J. E.: The pan-Arctic catchment database (ARCADE), *Earth Syst. Sci. Data*, 15, 541–
996 554, <https://doi.org/10.5194/essd-15-541-2023>, 2023.

997

998 Streletskiy, D. A., Suter, L. J., Shiklomanov, N. I., Porfiriev, B. N., and Eliseev, D. O.: Assessment
999 of climate change impacts on buildings, structures and infrastructure in the Russian regions on per-
1000 mafrost, *Environ. Res. Lett.*, 14, 025003, 2019.

1001

1002 Streletskiy, D. A., Clemens, S., Lanckman, J.-P., and Shiklomanov, N. I.: The costs of Arctic infra-
1003 structure damages due to permafrost degradation, *Environ. Res. Lett.*, 18, 015006, [https://doi.org/](https://doi.org/10.1088/1748-9326/acab18)
1004 [10.1088/1748-9326/acab18](https://doi.org/10.1088/1748-9326/acab18), 2023.

1005

1006 Stuenzi, S. M., Boike, J., Gädeke, A., Herzsuh, U., Kruse, S., Pestryakova, L. A., Westermann,
1007 S., and Langer, M.: Sensitivity of ecosystem-protected permafrost under changing boreal forest
1008 structures, *Environ. Res. Lett.*, 16, 084045, <https://doi.org/10.1088/1748-9326/ac153d>, 2021.

1009

1010 van Vuuren, D. P., Edmonds, J., Thomson, A., Riahi, K., Kainuma, M., Matsui, T., Hurtt, G. C.,
1011 Lamarque, J.-F., Meinshausen, M., Smith, S., Granier, C., Rose, S. K., and Hibbard, K. A.: The rep-
1012 resentative concentration pathways: An overview, *Climatic Change*, 109, 5–31, [https://doi.org/](https://doi.org/10.1007/s10584-011-0148-z)
1013 [10.1007/s10584-011-0148-z](https://doi.org/10.1007/s10584-011-0148-z), 2011.

1014

1015 Viers, J., Prokushkin, A. S., Pokrovsky, O. S., *et al.*: Seasonal and spatial variability of elemental
1016 concentrations in boreal forest larch foliage of Central Siberia on continuous permafrost, *Biogeo-*
1017 *chemistry*, 113(1-3), 435–449, <https://doi.org/10.1007/s10533-012-9770-8>, 2013.

1018

1019 Vitasse, Y., Porté, A. J., Kremer, A., *et al.*: Responses of canopy duration to temperature changes in
1020 four temperate tree species: Relative contributions of spring and autumn leaf phenology, *Oecologia*,
1021 161, 187–198, <https://doi.org/10.1007/s00442-009-1363-4>, 2009.

1022

1023 Vitasse, Y., François, C., Delpierre, N., Dufrêne, E., Kremer, A., Chuine, I., and Delzon S.: Assess-
1024 ing the effects of climate change on the phenology of European temperate trees, *Agricultural and*
1025 *Forest Meteorology*, 151(7), 969–980, ISSN 0168-1923, [https://doi.org/10.1016/](https://doi.org/10.1016/j.agrformet.2011.03.003)
1026 [j.agrformet.2011.03.003](https://doi.org/10.1016/j.agrformet.2011.03.003), 2011.

1027

1028 Vonk, J. E., Speetjens, N. J., and Poste, A. E.: Small watersheds may play a disproportionate role in
1029 arctic land-ocean fluxes, *Nat. Commun.*, 14, 3442, <https://doi.org/10.1038/s41467-023-39209-7>,
1030 2023.

1031

1032 Walvoord, M. A., and Kurylyk, B. L.: Hydrologic impacts of thawing permafrost—A review, *Va-*
1033 *dose Zone Journal*, 15, 1–20, <https://doi.org/10.2136/vzj2016.01.0010>, 2016.

1034

1035 Walvoord, M. A., and Striegl, R. G.: Complex vulnerabilities of the water and aquatic carbon cycles
1036 to permafrost thaw, *Front. Clim.*, 3, 730402, <https://doi.org/10.3389/fclim.2021.730402>, 2021.

1037

1038 Wang, J., and Liu, D.: Vegetation green-up date is more sensitive to permafrost degradation than
1039 climate change in spring across the northern permafrost region, *Global Change Biology*, 28, 1569–
1040 1582, <https://doi.org/10.1111/gcb.16011>, 2022.

1041

1042 Weller, H. G., Tabor, G., Jasak, H., and Fureby, C.: A tensorial approach to computational contin-
1043 uum mechanics using object orientated techniques, *Computers in Physics*, 12, 620–631, [https://](https://doi.org/10.1063/1.168744)
1044 doi.org/10.1063/1.168744, 1998.

1045

1046 Westermann, S., Barboux, C., Bartsch, A., Delaloye, R., Grosse, G., Heim, B., Hugelius, G., Irr-
1047 gang, A., Kääb, A. M., Matthes, H., Nitze, I., Pellet, C., Seifert, F. M., Strozzi, T., Wegmüller, U.,
1048 Wieczorek, M., and Wiesmann, A.: ESA Permafrost Climate Change Initiative (Permafrost_cci):
1049 Permafrost active layer thickness for the Northern Hemisphere, v4.0, NERC EDS Centre for Envi-
1050 ronmental Data Analysis, 24 April 2024, [https://doi.org/10.5285/
1051 d34330ce3f604e368c06d76de1987ce5](https://doi.org/10.5285/d34330ce3f604e368c06d76de1987ce5), 2024.

1052

1053 Wright, S. N., Thompson, L. M., Olefeldt, D., Connon, R. F., Carpino, O. A., Beel, C. R., and Quint-
1054 ton, W. L.: Thaw-induced impacts on land and water in discontinuous permafrost: A review of the
1055 Taiga Plains and Taiga Shield, northwestern Canada, *Earth-Science Reviews*, 232, 104104, ISSN
1056 0012-8252, <https://doi.org/10.1016/j.earscirev.2022.104104>, 2022.

1057

1058 Zellweger, F., Coomes, D., Lenoir, J., *et al.*: Seasonal drivers of understorey temperature buffering
1059 in temperate deciduous forests across Europe, *Global Ecol. Biogeogr.*, 28, 1774–1786, [https://
1060 doi.org/10.1111/geb.12991](https://doi.org/10.1111/geb.12991), 2019.

1061

1062 Zellweger, F., *et al.*: Forest microclimate dynamics drive plant responses to warming, *Science*, 368,
1063 772–775, <https://doi.org/10.1126/science.aba6880>, 2020.